High-Pressure neutron powder diffraction study of ε-CL-20: a gentler way to study energetic materials

Sumit Konar, Steven Hunter, Carole A. Morrison, Paul L. Coster, Helen Maynard-Casely, Jonathan G. Richardson, William G. Marshall, Annette Kleppe, Stewart F. Parker and Colin R. Pulham

Published version information

Citation: S Konar et al. 'High-Pressure neutron powder diffraction study of ε-CL-20: a gentler way to study energetic materials.' Journal of Physical Chemistry C, vol. 124, no. 51 (2020): 27985-27995.

DOI: 10.1021/acs.jpcc.0c09967

A High-Pressure Neutron Powder Diffraction Study of ε-CL-20: A Gentler Way to Study Explosives to Avoid Synchrotron-Induced Radiation Damage

Sumit Konar,*† Steven Hunter,† Carole A. Morrison,† Paul L. Coster,† Helen Maynard-Casely,† Jonathan G. Richardson,† William G. Marshall,‡ Annette Kleppe,§ Stewart F. Parker,‡ and Colin R. Pulham†

†EaStCHEM School of Chemistry and Centre for Science at Extreme Conditions, The University of Edinburgh, King's Buildings, David Brewster Road, Edinburgh EH9 3FJ, U.K.

‡ISIS Neutron and Muon Facility, STFC Rutherford Appleton Laboratory, Harwell, Oxford, Didcot, Oxfordshire OX11 0QX, U.K.

§ Diamond Light Source, Rutherford Appleton Laboratory, Harwell Science and Innovation Campus, Didcot, Oxfordshire, OX110QX, England, U.K.

KEYWORDS. Neutron diffraction, equation of state, high pressure, energetic materials, radiation damage

ABSTRACT: High-pressure studies have been performed on the ε-form of the powerful explosive CL-20. Hydrostatic compression over the pressure range 0-12 GPa has been monitored using synchrotron powder X-ray diffraction. The potential effects of X-ray radiation damage were observed and circumvented through a follow-up compression study over the pressure range 0-7 GPa using neutron powder diffraction. This second study revealed smooth compression behaviour, and the absence of any phase transitions. Intermolecular interaction energies as obtained using PIXEL calculations did not show any discontinuity upon application of pressure. An isothermal equation of state has been determined, and the high-pressure response is supported by dispersion-corrected DFT calculations. Inelastic neutron scattering (INS) (experimental and simulated) spectra for the ε-form are in excellent agreement.

1. INTRODUCTION

Energetic materials (EMs) are compounds with high amounts of stored chemical energy and are widely used in vehicle airbag inflators, rocket propellants, civil constructions and defence applications.[1,2] Detonation involves a complex combination of chemical, mechanical and physical processes. Understanding such complex and rapid processes is challenging, but is key to the design and safe use of EMs. Estimates of chemical kinetics, reaction mechanisms and high-pressure, temperature, thermodynamic properties are crucial to model more realistic detonation events. Extrapolations made from data derived from ambient conditions are often unreliable, and so in order to reduce modelling uncertainties it is essential to measure thermodynamic properties of explosives under pressure. Moreover, pressure is known to induce structural changes (polymorphism) in molecular materials, which introduces further uncertainties in energetic behaviour. Molecular EMs, including FOX-7,[3] HMX,[4,5] RDX,[6–8] and TATB[9] have all been carefully investigated using high-pressure, and many of them have shown pressure-induced phase transition behaviour.

This study concerns the effect of pressure on one of the most powerful explosives in current use: CL-20, so-called due to its development at China Lake, USA. It is a polycyclic nitramine (2,4,6,8,10,12 hexanitrohexaaza-isowurtzitane) with six nitro groups bonded to an isowurtzitane cage (see Figure 1(a)). First synthesised in 1987, the detailed synthetic procedure was only published in 1998.[10] The inherent strain in the isowurtzitane cage, along with the increased density (with respect to its monocyclic analogue), and low ratio of carbon atoms to nitramine moieties render CL-20 as one of the densest (2.04 g/cm^3) and most energetically explosive (detonation velocity 9500 km/s) compounds in current use. To date, a significant amount of computational and experimental research has been conducted to evaluate the explosive performance,[11] sensitivity[12] and thermal properties[13–15] of CL-20. In general, the high sensitivity of CL-20 makes it unsafe for many practical applications in its pure form, although its sensitivity has been reported to be reduced through the addition of a plasticizer, and the resulting composite form has demonstrated success as a rocket propellant.[16]

Considering steric hindrance and the mutual repulsion of the nearest oxygen atoms, only eight

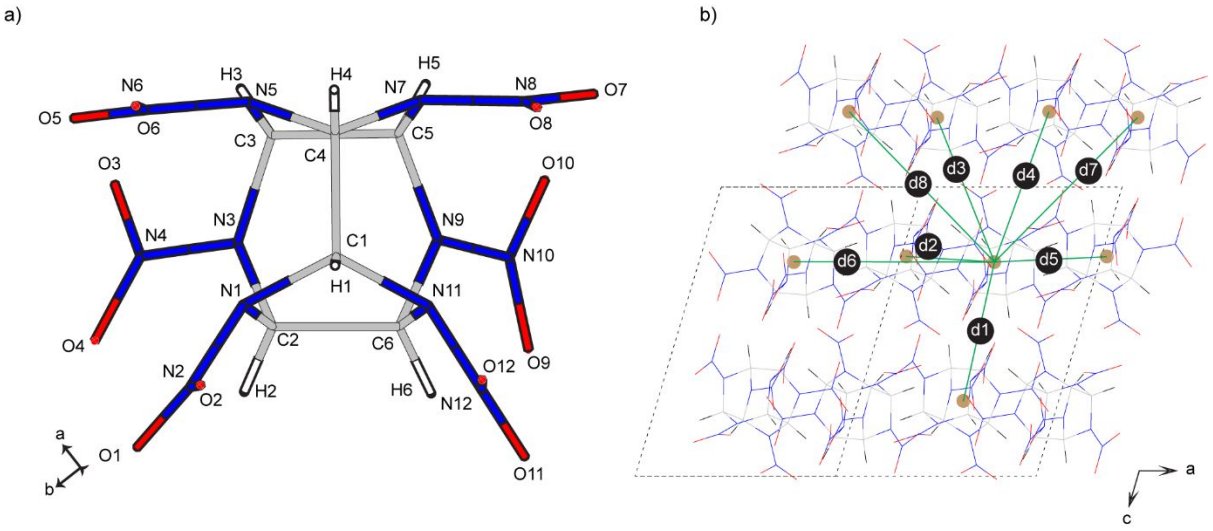

Figure 1 a) Molecular structure of ε-CL-20 ($C_6N_{12}H_6O_{12}$); b) the unit cell of ε-CL-20 (Z=4), intermolecular centroid distances (d1-d8) are labelled in order of increasing magnitude.

conformers are found to be stable out of a possible 24 configurations.[13] FTIR spectroscopy and single-crystal X-ray diffraction revealed four crystalline phases (the α-, β-, γ- and ε- forms) at ambient pressure.[17] The six N–NO_2 bonds of the CL-20 molecule are quite flexible; and the six wag angles (δ1- δ6, named with respect to increasing nitrogen atom numbering, i.e. the angle between N1-N2 and the C1-N1-N2 plane, etc, see Figure S1, ESI for more details) are distinct in different conformers. The four structurally characterized forms correspond to the three most stable isolated molecule conformations, as determined by DFT calculations.[18] The ε-form (monoclinic, space group $P2_1/n$, see Figure 1(b)) is found to be the densest and is the most stable form under ambient conditions. It is often precipitated as the final product of the synthesis. The α-form has been shown to be a hydrate, rather than a true polymorph of CL-20. This form (orthorhombic, space group *Pbca*) along with the β-form (monoclinic, space group $Pb2_1a$) can be obtained by re-crystallization of the crude product in conc. HNO_3 and benzene, respectively.[10] Russell et al reported that upon heating to 428-471 K, the α-, β-, and ε-forms all undergo an endothermic transition to the γ form.[17] They also identified a new high-pressure ζ-form ($P2_1/n$) while compressing the γ-form above 0.7 GPa which could not be retrieved at ambient pressure. The structure of the ζ-form was later determined using a combination of single crystal X-ray and powder diffraction techniques by Millar et al.[19]

Herein, we focus on the stable ambient pressure ε-form of CL-20. While there have been several reports on the vibrational spectra of the various polymorphs of CL-20,[20–24] to date there has been no thorough analysis offering a complete listing of the fundamental modes. Characterization of the low energy lattice mode region has recently been highlighted as being of fundamental importance in predicting the impact sensitivity behavior of energetic compounds.[25,26] These data can be obtained by inelastic neutron scattering (INS) measurements and simulated using density functional theory (DFT) condensed matter simulations. The former provides benchmark data for the latter, which then permits full characterization of the experimental data, such as assignment of the individual vibrational eigenvectors.

A previous experimental compression study on the ε-form has been performed by Gump et al, who reported an absence of any phase transition up to 5.6 GPa at ambient temperature.[27] The pressure transmitting medium (PTM) used in their study was Dow Corning Fluid 200 (1cSt, silicone oil), which only remains truly hydrostatic up to pressures of ~0.9 GPa, thus warranting a re-investigation. A vibrational spectroscopy study using helium as a PTM was later conducted by Ciezak et al,[28] who observed intensity changes and discontinuities in the pressure shifts of vibrational modes which hinted towards two potential pressure-induced phase transitions: the first (proposed as ε → γ) occurred between 4.1 and 6.4 GPa, and the second (proposed as γ → ζ) occurred near 18.7 GPa. These apparent discrepancies in the high-pressure behaviour of CL-20 may arise in part from the different experimental techniques and conditions used. The literature also appears to report two different pressures to access the ζ phase: 0.7 GPa[17] by Russell et al starting from the γ-phase, and 18.7 GPa by Ciezak et al starting from the ε-form. Previously we also conducted a high pressure XRD study on polycrystalline ε-CL-20 and did not observe any phase transformation up to 7.2 GPa.[29] X-ray powder diffraction studies of organic solids are often hindered by the low atomic number of their constituent atoms (C, H, N, O). This can be

circumvented through the use of neutron diffraction techniques, which have become important tools for the study of molecular explosives.[30]

CL-20 has been extensively studied using various modelling techniques. Molecular dynamics (MD) simulations have been used to calculate the lattice parameters and equations of state for the four polymorphs of CL-20.[31] A more recent MD study, using a flexible-molecule force field, did not observe the $\varepsilon \rightarrow \gamma$ phase transition.[32] Similarly, multiple DFT studies on crystalline CL-20[33–35] have also noted the absence of a phase transition over low (0–2.7 GPa)[33,35] and high (up to 75 GPa)[36] pressure ranges. With an apparent discrepancy between simulation and experiment (and disagreement between experiments) a new investigation into the pressure response of this important energetic material is now warranted.

The objectives of this research effort are therefore to (i) perform the first inelastic neutron scattering studies on ε-CL-20, ii) to assign the vibrational (phonon) density of states using DFT-D simulations, iii) to undertake a hydrostatic compression study of CL-20 using powder XRD to check the validity of the pressure induced transition as observed in the spectroscopic study, iv) to conduct the first neutron powder diffraction study to facilitate the calculation of an improved equation of state (EoS) of ε-CL-20, and v) to rationalize the change in intermolecular interactions upon application of pressure using PIXEL calculations.

2. EXPERIMENTAL AND COMPUTATIONAL METHODS

2.1 Sample Preparation. Crystalline samples of ε-CL-20 used for X-ray diffraction and neutron diffraction studies were kindly provided by Dr. Bernard Garatay (QinetiQ, Fort Halstead).

2.2. X-ray Powder Diffraction. High-pressure X-ray powder diffraction (XRPD) experiments were conducted on beamline I15 at the Diamond Light Source at Harwell Campus, UK. Finely ground powders of polycrystalline ε-CL-20 were loaded into diamond-anvil cells (DAC) of Merrill Bassett type with 600 μm diameter culets.[37] The samples were contained within 250 μm thick tungsten gaskets (pre-indented to a thickness of 100–150 μm with a 300 μm hole), along with 2-3 μm diameter ruby spheres included for pressure measurement.[38] A 4:1 methanol:ethanol mixture, known to maintain hydrostaticity up to 10 GPa,[39] was used as the PTM. The X-ray beam was collimated to a diameter of 50 μm and samples were exposed for 60 s. The distance between the sample and detector was optimised in each case to obtain the maximum amount of crystallographic information. Data were collected on two-dimensional MAR345 image plates, integrated and reformatted using Fit2D,[40] and then exported to GSAS for Rietveld refinement.[41] This proceeded according to the following strategy: i) a background data fit was obtained using a shifted Chebyshev polynomial function, ii) a peak shape fit was performed using a pseudo-Voigt shape function (type 2 in GSAS), iii) initial unit cell parameters were obtained from ambient pressure crystal structure[10], and refined, iv) atomic positions were refined, treating CL-20 as a rigid body, and finally v) where possible, thermal displacement parameters (Uiso) were refined though constraining all like atoms.

2.3 Neutron Powder Diffraction (NPD) High-pressure time-of-flight (ToF) neutron powder diffraction (NPD) experiments were conducted at the UK spallation neutron source, ISIS, at the STFC Rutherford Appleton Laboratory using the PEARL/HiPr diffractometer.[42] Due to the complexity of the synthetic procedure, a deuterated sample of ε-CL-20 could not be obtained, but the small percentage of hydrogen in the sample gave rise to only a very low incoherent scattering. A lightly ground sample (ca. 100 mg) of ε-CL-20 was loaded into an encapsulated null-scattering TiZr gasket, together with a small amount of 4:1 perdeuterated methanol/ethanol as the PTM and a sample of lead as the pressure calibrant.[43] The assembly was then compressed with a type V3b Paris–Edinburgh (P–E) press,[44] equipped with standard single toroidal zirconia-toughened alumina (ZTA) anvils. Sample pressures were calculated from the refined lead lattice parameters with an uncertainty of ± 0.05 GPa. Data collection times per pressure point ranged between 1 and 6 hours. ToF NPD data were collected using the $2\theta = 90°$ detector bank with a transverse (through-anvil) scattering geometry. The resulting summed pattern was then normalised with respect to the incident beam monitor and the scattering from a standard vanadium calibration sample using MANTID.[45] Lastly, the diffraction pattern intensity scale was corrected for the wavelength and scattering-angle dependence of the neutron attenuation by the anvil (ZTA) and gasket (TiZr) materials. Full-profile Rietveld refinements of the ToF NPD patterns were carried out using the GSAS package.[41] Parameters obtained from instrument calibration was not refined. Pseudo-Voigt function is a linear combination of Gaussian (σ terms) and Lorentzian functions (γ terms) and only two parameters σ1 (sig-1), and γ1 (gam-1) were refined. Constraints were imposed such that thermal vibration parameters are refined collectively for each atom type. Unlike the XRPD study now all Uiso values could be successfully refined throughout the whole pressure range.

2.4 Inelastic Neutron Scattering. INS spectra (24-4000 cm^{-1}) were recorded using the TOSCA instrument[46] at the ISIS Neutron and Muon facility, which has an energy resolution of ~1.25%. Approximately 2.5 g of polycrystalline ε-CL-20 was loaded into an aluminium sample can and cooled to $T < 20$ K in a conventional closed cycle refrigerator. Spectra were recorded for 3–6 h. INS data were visualised and compared to the simulated spectra of the DFT-D calculations using the aCLIMAX program.[47]

2.5 Computational methods. Structure optimisations (at ambient pressure and under externally applied hydrostatic pressure conditions) and vibrational frequency calculations were performed using density functional theory plus dispersion (DFT-D) and the plane-wave pseudopotential method as implemented in CASTEP version 5.5,[48] utilising the dispersion correction scheme of Grimme[49] coupled to the PBE functional.[50] On-the-fly (OTF)[51] pseudopotentials and a plane-wave cut-off energy of 650 eV was used throughout, which ensured convergence of both lattice parameters and total energies to less than 5 meV per atom. Brillouin zone sampling was obtained using an MP[52] grid of 2 × 2 × 2 (2 k-points). The structures were relaxed using the BFGS method[53] to allow both atomic coordinates and unit cell vectors to optimise simultaneously while constraining space group geometry (convergence criteria: maximum change in system energy = 2×10^{-5} eV, maximum RMS force = 0.025 eV Å^{-1}, maximum RMS stress = 0.01 GPa and maximum RMS displacement = 0.002 Å). Following successful geometry optimisation of the experimental starting structure, external hydrostatic pressures were applied at pressures corresponding to experimental data. Phonon frequencies (at the gamma point in k-space) for the optimised structures were then calculated by finite displacement methods.

2.6 PIXEL method. Intermolecular interaction energies and lattice energies (broken down into constituent Columbic, polarisation, dispersion and repulsion contributions) were determined using PIXEL calculations,[54–57] facilitated by the MrPIXEL automation tools.[58] In this study the cluster radius was 15 Å, and the molecular electron densities were obtained from GAUSSIAN-09[59] utilising the 6-31G** basis set at the MP2 level of theory. The PIXEL calculations themselves were performed using the CLP-PIXEL suite.[57] The electron densities were calculated on a grid of dimensions 0.08 × 0.08 × 0.08 Å^3; subsequent energy calculations employed a level 4 condensation grid.

3. RESULTS AND DISCUSSION

3.1 Ambient-pressure computational structure. ε-CL-20 crystallises in the monoclinic crystal system ($P2_1/n$, Z=4), and the experimental unit-cell volume at ambient pressure varies between 1397.2 (at 100 K) and 1430.2 Å^3 (at 298 K).[60] A DFT calculation by Xu et al.[34] overestimates the cell volume by 4.2 % due to the omission of van der Waals (vdW) dispersion interactions; including the semi-empirical correction term (proposed by Grimme) significantly improves the calculation accuracy, with the deviation now amounting to just 0.3 %.[35] Our results (using the same DFT-D scheme) are reported in TABLE S1, alongside previous experiment and dispersion-corrected DFT studies (DFT-D) and the results obtained from two molecular dynamics (MD) studies using classical force fields. All our calculated lattice parameters agree with experiment[60] to within 0.6%, and the overall unit cell volume differs from experiment by just 1.7%. These results are broadly consistent with a previous DFT-D study.[35] The six wag angles (δ1-δ6) obtained from our DFT calculations are in excellent agreement with the values obtained from the experimental structure (in parenthesis): 36°(40°), 1°(1°), 28°(30°), 29°(33°), 19°(24°), and 37°(40°), as expected for the ε-form. For comparison, the values expected for the γ-form[60] are 36°, 40°, 15°, 37°, 49° and 28°, indicating that the molecular structures in the two different polymorphs are geometrically distinct. To summarize, our computational studies are able to predict unit-cell dimensions in close agreement with experimental values.

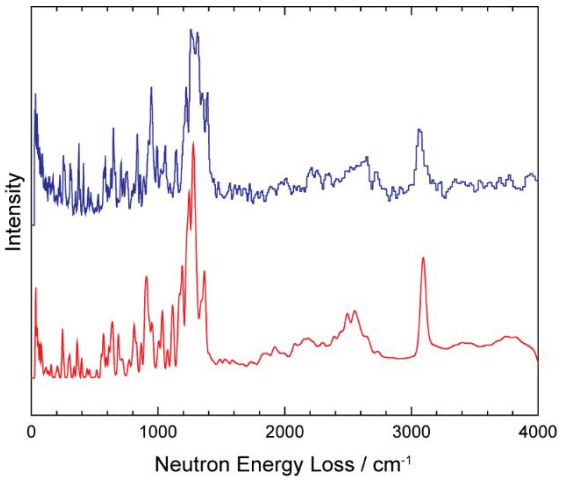

Figure 2. Experimental (blue) and computed (red) INS spectra of ε-CL-20.

3.2 Vibrational Properties. The experimental INS spectrum is shown in Figure 2 alongside the DFT-D computed spectrum. The majority of the calculated fundamental vibrational modes are in good agreement (<2.5% difference) with experiment. Computed phonon density of states (Brillouin zone Γ-point) for ε-CL-20 is shown in Figure S2, ESI. A full assignment of the calculated phonon density of states is given in Table S3. A comparison of the calculated fundamental modes for ε-CL-20 with the experimental INS spectra determined in this study is shown in Table S4, ESI. From this analysis it is apparent that the character of the lattice modes near the top of the phonon bath region of the density of states (*ca.* 175 cm^{-1}) is dominated by NO_2 amalgamated modes. This is in keeping with other EMs that are sensitive to impact initiation.[26]

3.3 High pressure computational structures. The ambient pressure unit cell was compressed up to 7.2

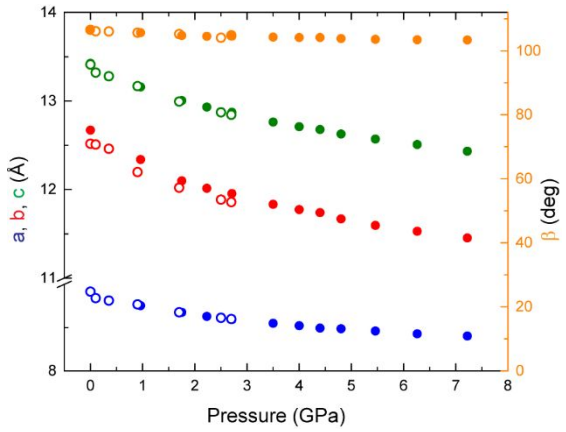

Figure 3 Lattice parameters as a function of hydrostatic pressure. Solid circle: DFT-D (this work), open circle: DFT-D Ref 35. Blue: *a*-axis, red: *b*-axis, green: *c*-axis, orange: *β*-angle.

GPa. The variations in the unit cell parameters are given in Table S5 (ESI), and plotted in Figure 3. An overall smooth compression trend is observed up to 7.2 GPa, with ε -CL-20 showing close to isotropic compressibility ($b/b_0 = 0.90$, $c/c_0 = 0.93$, $a/a_0 = 0.94$); this relative compressibility trend agrees with previous computational studies.[35,36] From our DFT-D study, and the growing wealth of other recent computational studies,[31–34,36] it is evident that the pressure-induced ε to γ transition is not observed. The six N–NO_2 groups of the ε-CL-20 molecule are quite flexible, and it is known that the orientation of the nitro groups change with applied pressure.[32] Values for the δ1-δ6 from the optimized pressure structures are given in the ESI (Figure S1 and Table S2, ESI), from which a smooth trend is evident for all angles with the exception of δ4, which shows a pronounced change above 4.4 GPa. The absolute magnitude of the angle change does not exceed 4° however, but it may potentially account for the subtle changes observed in the previous vibrational spectroscopy study.[28,61]

3.4 High-Pressure X-ray Powder Diffraction. In order to extend the pressure range of previous diffraction studies,[27] we conducted our 1st compression experiment[29] at beamline I15 at the Diamond Light Source, and high quality XRPD data were obtained (using λ = 0.4847 Å) up to 7.2 GPa. The aim of this experiment was to critically examine the proposed transition to the γ-form which had been observed spectroscopically.[28] Figure 4 shows the quality of Rietveld fit at nearly ambient pressure (the 'as loaded' sample) and at 7.2 GPa; from this it can be confirmed that the sample did not react with moisture or air prior to loading, and also did not react with the PTM. While the quality of the Rietveld fit at ambient pressure was excellent (Rwp = 6.06), the same could not be said for the best fit obtained for the highest pressure data set (Rwp = 20.29). Crystallographic indices *hkl* at higher *d*-spacing range were also shown for qualitative comparison of the Bragg reflections of PXRD patterns at two different pressures, and it shows no evidence of formation of any new phase. This set of experiments allow us to reliably confirm that the ε-form remains stable and does not underdo a phase transition in the 4.1 – 6.4 GPa pressure regime, in contrast to the previous report.[28]

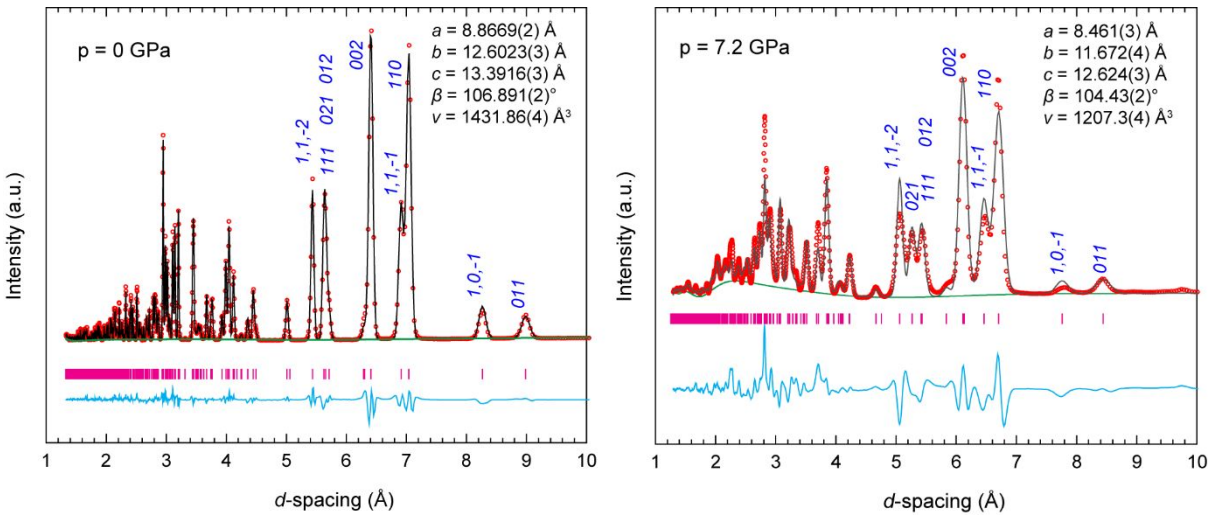

Figure 4. Rietveld refinements of the X-ray powder diffraction pattern using ε-CL-20 as the structural model. Left: measured at ambient pressure (~0.0001 GPa); Right: measured at 7.2 GPa; some characteristic Bragg reflections are labelled for visual comparison of the two XRPD patterns.

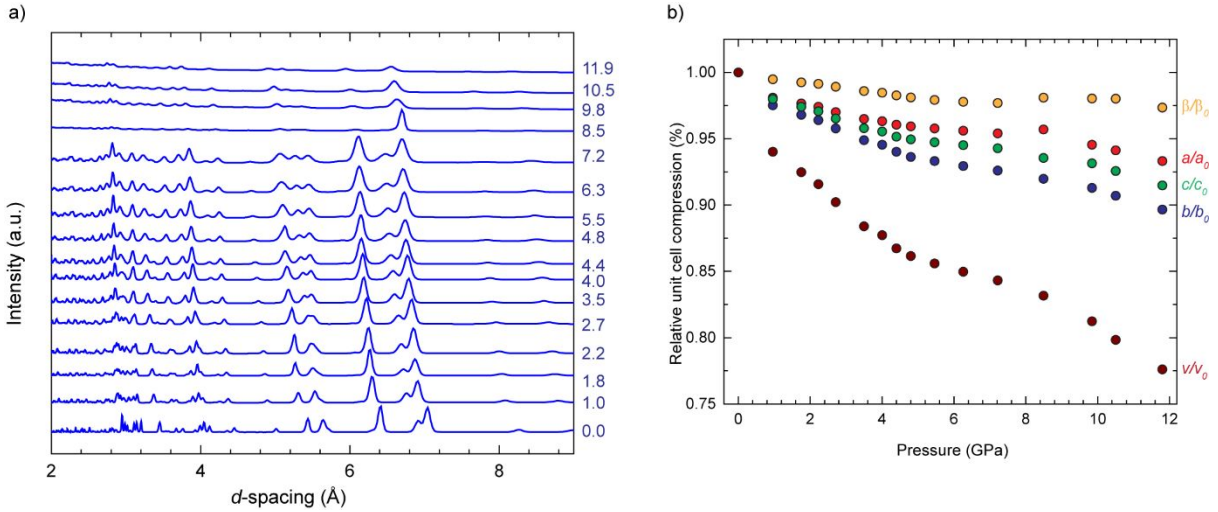

Figure 5. a) Sequence of XPRD patterns obtained for ε-CL-20 upon increasing pressure; b) Relative unit cell compression (%) of ε-CL-20 from current XRPD study under hydrostatic condition.

Our second set of compression experiments were conducted at the same beamline, in an almost identical set up to the previous experiments, with the exception that a slightly higher energy (λ = 0.3727 Å) X-ray radiation source was used. The polycrystalline sample was loaded and the phase purity of the sample was checked. The sample was then compressed beyond 7 GPa and up to 11.8 GPa, thereby considerably extending the pressure range to search for the potential phase transition to the γ-phase. Data collection above 11.8 GPa was prevented by sudden violent decomposition of the sample upon further compression, evident from an audible click from the DAC. Analysis of the contents of the gasket after this event showed the sample chamber retained some pressure (*ca.* 6 GPa). While the quality of the data at pressures above 7 GPa was poor compared to the 1st compression experiment, it was good enough to obtain reliable lattice parameters, and all data sets could be refined using ε-CL-20 as a structural model (see Figure 5).

The compression behavior of the unit cell axes are shown in Figure 5b, and reported in Table S6. All the refinement plots are shown in Figure S3, ESI. As expected, the overall compressibility trend between 0-7.2 GPa largely mirrors the report from the first (lower X-ray intensity study), with $b/b_0 = 0.93$, $c/c_0 = 0.94$, $a/a_0 = 0.95$, while between 0-11.8 GPa the lattice vectors vary as $b/b_0 = 0.90$, $c/c_0 = 0.91$, $a/a_0 = 0.93$. The most interesting aspect to note in this study is that the variation in the lattice parameters with pressure do not follow an overall smooth trend, as observed in our DFT-D calculations (Figure 3). The gradients of relative contraction for the three lattice parameters decrease around 5 GPa; this may be indicative of a subtle adaptation of either the compression mechanism or a change in the structure itself in this pressure regime. Full profile Rietveld refinements of all the subsequent patterns using the ε-CL_20 structure confirmed that the absence of any phase transition. The calculated XRPD patterns of γ-form and ε-form are compared in Figure S4, ESI, from which it could be ascertained that the characteristic diffraction peaks arising from γ-form were not observed in this data set. This apparent discrepancy between theory and experiment prompted a complementary high pressure neutron powder diffraction study.

3.5 High-Pressure Neutron Powder Diffraction.

Experiments were performed over the pressure range 0 – 7.1 GPa. Results are shown in Figure 6, with the good quality of Rietveld fit (Figure 6a, the ' as loaded ' sample at near ambient pressure) confirming that the sample did not react with moisture or air prior to loading, and also did not react with the PTM. The lattice parameters obtained at near-ambient pressure closely mirror the values obtained from the XRPD data [NPD: a = 8.8629(9), b = 12.596(2), c = 13.380(1) Å, β = 106.917(8)°, V = 1429.0(2) Å^3; and XRPD: a = 8.8669(2), b = 12.6023(3), c = 13.3916(3) Å, β = 106.891(2) °, V= 1431.87(4) Å^3]. The additional reflections observed in the NPD patterns correspond to Pb (the pressure calibrant), Al_2O_3 (the gasket material), and ZrO_2 (the anvil material), as marked in Figure 6a and 6b. The quality of the Rietveld fit of NPD data both at ambient pressure and at 7.2 GPa is satisfactory (Rwp = 2.29 and 4.94, respectively). The pressure series of NPD patterns collected for ε -CL-20 up to 7.1 GPa are shown in Figure 6c; all the refinement plots are shown in Figure S5 and corresponding refinement data are included in Table S7, ESI. In keeping with our HP XRPD studies discussed above, all data collected in this pressure series could be fitted to the ε-form of CL-

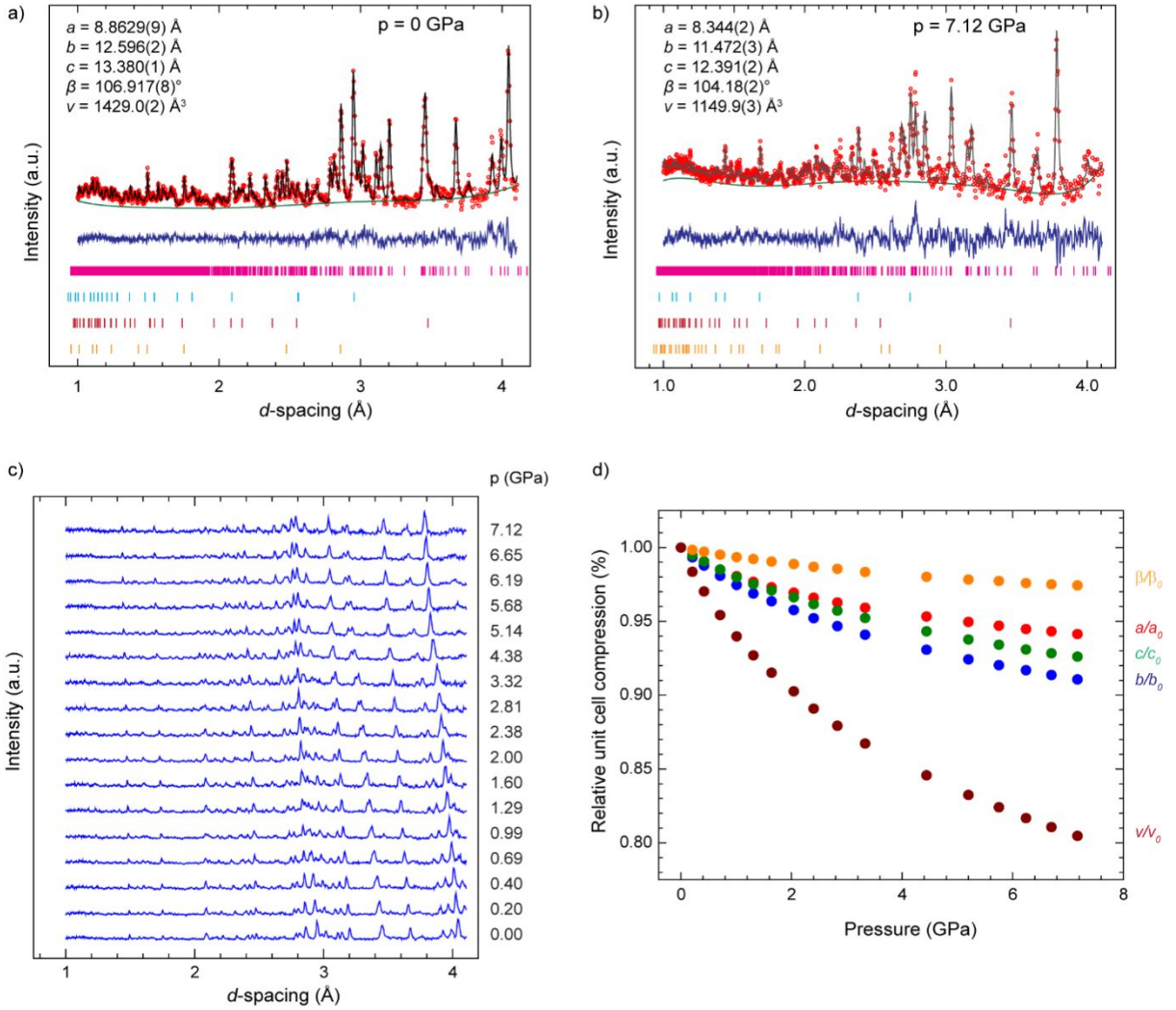

Figure 6. a), b) Rietveld refinement of neutron diffraction for ε CL-20 at ambient pressure (0.0001 GPa) and at 7.12 GPa;, experimental (obs) data are shown as red dots, the solid black and green line show the calculated profile from Rietveld refinement and background fit, respectively, and the bottom blue trace shows the residual intensity (I), I(obs)-I(calc). The simulated Bragg reflections for each phase are given as vertical lines; from top to bottom ε CL-20, Pb, Al_2O_3 and ZrO_2; c) sequence of NPD patterns obtained upon increasing pressure; d) Relative unit cell compression (%).

20, and no transition to the γ-form between 4.5 and 6.4 GPa as previously proposed was observed.[28]

The compression behavior of the unit cell axes is shown in Figure 6d, which shows broadly similar behavior to that obtained in the HP XRD studies between 0-7.2 GPa ($b/b_0 = 0.91$, $c/c_0 = 0.93$, $a/a_0 = 0.94$). While the general trends are consistent, differences are apparent at the highest pressure point (7.2 GPa), with a larger unit cell recorded by the XRPD data [NPD: a = 8.344(2), b = 11.472(3), c = 12.391(2) Å, β= 104.18(2)°, V = 1149.9(3)Å^3; XRPD: a = 8.461(3), b = 11.672(4), c = 12.624(3) Å, β = 104.43(2)°, V= 1207.3(4) Å^3]. While it is quite evident that the initial lattice parameters were consistent in both experiments, ε-CL-20 appears to have behaved differently at higher pressures in the X-ray beam compared to the neutron beam: the kinks observed in the X-ray study are not present in the neutron study.

Since the ε-CL-20 used in the NPD study was not deuterated, we can rule out this factor as a potential cause for the differences in compression behaviour observed between the high pressure X-ray and neutron studies. Likewise, the same PTM was used in both studies, ruling out possible differences in hydrostaticity or reactions with the PTM as the underlying cause. This leaves the radiation source as the only significant variable between the two experiments, and thus the logical reason for the disparity in results is that the incident high flux of the synchrotron X-rays induced radiation damage in the ε-CL-20 sample. We note a recent report of a similar event.[62]

3.6 Further investigation into the XRPD and NPD study discrepancies. Our concerns on X-ray induced radiation damage for ε-CL-20 were confirmed

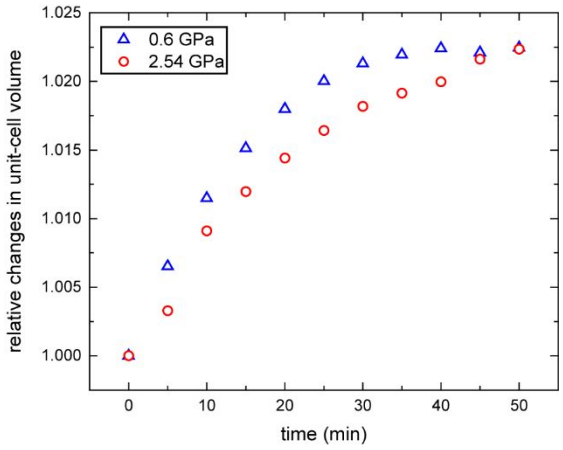

Figure 7. Increase in unit-cell volume due to Radiation damage over time.

by a further set of experiments at the same synchrotron source, where samples were compressed to 0.6 and 2.5 GPa, respectively and then repeatedly exposed to prolonged irradiation with high-flux X-rays (λ=0.4119 Å). Figure 7 clearly shows that there are significant changes in unit cell volumes even after short time periods. The relative changes caused by radiation damage are similar at both pressures. These increases in unit cell volume will lead to errors in the equation of state, as the volume change will not be solely due to the changes in pressure, but rather a combination of the effects of pressure and radiation damage. Hence we attribute the anomalous data from the high-pressure X-ray diffraction experiment to localized radiation damage of the sample. The increase in the lattice parameters is also likely to be caused decomposition products being trapped in interstitial positions or voids in the crystal lattice.

3.7 The Equation of State for ε-CL-20. Figure 8a shows the variation of unit-cell volume for ε-CL-20 as a function of pressure, as determined in this work by NPD, XRPD and DFT-D simulations. While the unit-cell volume calculated from the simulation is slightly larger than the values obtained from the NPD experiment, the hydrostatic compression trend predicted by the DFT-D method is in excellent agreement with the compression trend determined from the NPD experiment. The model derived from the X-ray data deviates strongly from this line at above 2 GPa. Figure 8b compares our NPD data with the previous XRPD data obtained from Gump and Periis,[27] which clearly shows that the earlier XRPD has significantly larger errors (due to non-hydrostatic conditions) and also significantly higher unit cell volumes than our NPD data. Given the outcomes of our radiation damage study (Figure 7), it is likely that this earlier study using synchrotron source with a monochromated X-ray beam (λ=0.49595 Å), also incurred significant radiation damage.

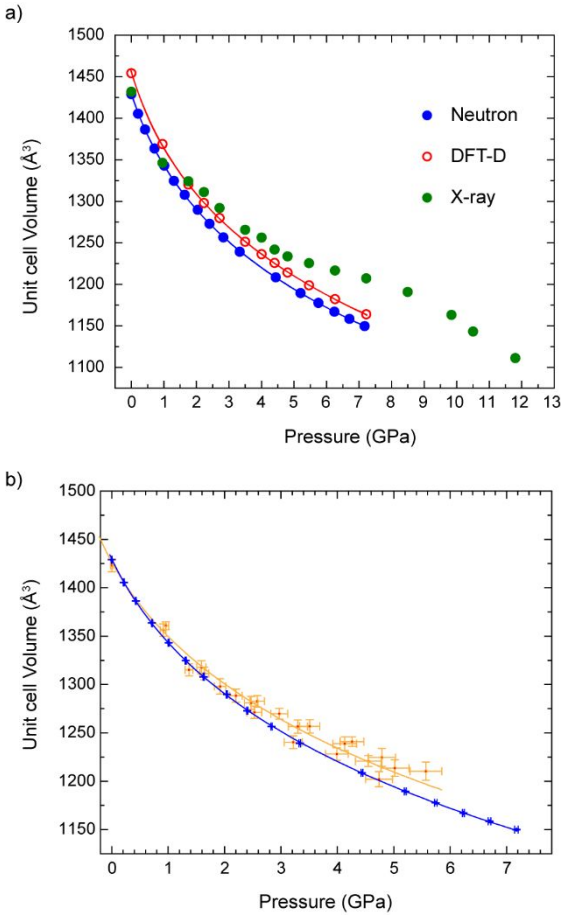

Figure 8. a) Unit cell volumes as a function of pressure for ε-CL-20; solid blue circles: current NPD data, solid green circles: current XRPD data, DFT-D is shown with small open red circles; both the NPD and DFT data are fitted with BM-3rd equation of state; b) comparison of *P-V* curve between NPD (this work) and previous XRPD study.[27]

The overall compression trends shown in Figure 8a were fitted with a 3rd order Birch–Murnaghan (BM-3) EoS. This equation relates the pressure (P) at a given volume (V) to the ambient pressure volume (V_o), the bulk modulus (B_0) and the derivative of the bulk modulus (B'). B_0 and B' values are determined from the current NPD data and DFT-D data from this work, along with the previous experimental XRPD (Gump & Peiris)[27], and previous computational DFT-D study.[35] We have used P and V data from previous studies and re-calculated B_0 and B' values, to compare all values in the same manner wherever possible. All the determined EoS values are presented in Table 1. From this we note that the B_0 value arising from the NPD study is very close to the values obtained from the DFT-D studies (current and previous work[35]), and the variation of bulk moduli are only within ~1 GPa of each other. In our work we compared B_0 and B' by both fixing V_0 to initial values and also allowing it to refine during EOS fitting; we noticed the bulk modulus values remain similar in

Table 1: Comparison of bulk moduli (B_0) and its pressure-derivative (B') determined from the EOS analyses of ε-CL-20. Values are shown in italics when V_0 is not refined. Approximate errors are shown for our work; the experimental pressure and volume errors are also used to estimate the standard errors for calculated values.

	V_0 (Å^3)	B_0 (GPa)	B′
NPD (this work)	1430.04(83)	11.49(20)	11.16(23)
	1429	11.72(9)	10.94(13)
DFT-D (this work)	1457(3)	10.27(56)	12.13(61)
	1454.23	10.81(17)	11.62(28)
DFT-D (Ref[35])	1433(3)	12(1)	10(2)
	1434.68	11.61(76)	11(2)
XRPD (Ref[27])	1427(8)	13(3)	11(3)
	1425.87	14(1)	11(2)

both cases. The previously determined B_0 value from non- hydrostatic XRPD data is found to be slightly higher with larger standard deviations, and this can be rationalized when the volume increase due to radiation damage is factored in. In our previous report[29] we found B' is substantially larger than any other experimental or theoretical study, but this can now be attributed to radiation damage affecting the reliability of unit cell volume response to increasing pressure.

3.8 The effects of pressure on intermolecular interactions. To complete this study, we have also explored the effect of pressure on the strength of the nearest neighbor intermolecular interactions using PIXEL calculations. The total interaction energies as a function of pressure are shown in Figure 9(a), where the total molecule–molecule energies (E_{tot}) or lattice energy (E_{lat}) are broken down into Coulombic (E_{coul}), polarisation (E_{pol}), dispersion (E_{disp}) and repulsion (E_{rep}) terms. The lattice energy steadily weakens (approaches and surpasses zero) as the molecules are forced into closer proximity with increasing pressure; this result is expected as the destabilizing repulsion contributions outweigh the combined stabilizing contribution of the other three terms. All components of the bonding interactions become increasingly more stable with increasing pressure, but this effect is cancelled out by the energy repulsion term, which dominates at pressures > 5 GPa, such that the total lattice energy becomes positive (Figure 9(a)); a similar observation has been reported in a previous study.[63] This suggests that a lower energy polymorph likely exists at high pressure, but it cannot be accessed through direct compression of the ε-CL-20 form, which in turn suggests that a kinetic barrier must be overcome for the phase transition to occur. Figure 9(b) shows molecular interaction energies as a function of molecular centroid separation for eight separate centroid-centroid distances, with the data point on the far right in each cluster representing the ambient pressure structure data, and those on the far left the highest pressure (*i.e.* most compressed) structure. Definitions for d1-d8 are highlighted on Figure 1b; and another clear representation is given on Figure S6, ESI. All contacts (except the longest (and weakest) contact, d8) follow a very similar trend, steadily destabilizing (becoming more positive) with increasing pressure. All contacts rest with positive interaction energies by the final high pressure structure, with the exceptions of d4, d6 and d8 which remain weakly attractive. The lack of any apparent discontinuities in this data again indicates that there is no phase transition over this pressure range.

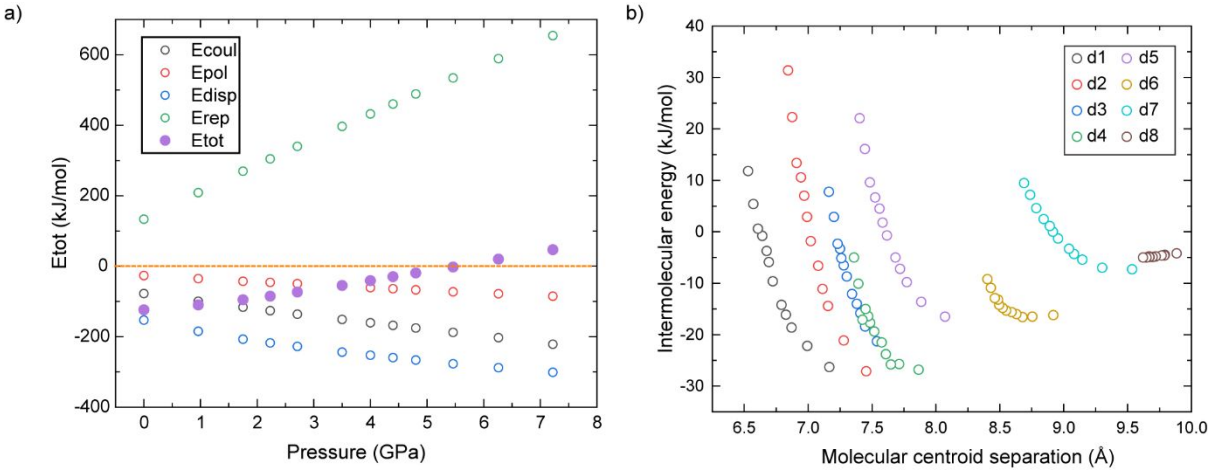

Figure 9. a) Effect of pressure on intermolecular interactions; b) Molecular interaction energies as a function of molecular centroid separation, obtained for the DFT-D optimised structures over the pressure range 0-7.2 GPa.

4. CONCLUSIONS

This work reports the effects of hydrostatic compression on the crystal structure of ε-CL-20. At ambient pressure our DFT-D model predicted all of the lattice parameters of ε-CL-20 to within 0.6% of experiment and our results are commensurate with previous modelling reports. Subsequent phonon calculations generated an INS spectrum which is in excellent agreement with our experimental spectrum. The character of the lattice modes at the top of the phonon bath are dominated by amalgamated NO_2 wag motions, in common with other EMs that are highly sensitive to shock impact initiation. The smooth compression trend produced by the neutron powder diffraction study was in excellent agreement with the hydrostatic compression trend predicted by the DFT-D method. No apparent discontinuities in the intermolecular energies further supports the lack of phase transition over this pressure window. The small, yet pronounced variation of one of the N-NO_2 wag angle may potentially account for the subtle changes as observed in the previous Raman study between 4 and 6 GPa. The combination of DFT-D and neutron results confirmed that the X-ray powder diffraction study did not produce results consistent with hydrostatic compression, and furthermore established that the ε-CL-20 sample was subjected to radiation damage during the high pressure X-ray study. The excellent match between our neutron diffraction results with computational findings shows the importance of performing high-pressure NPD for the study of structural evolution with pressure for energetic material.

ASSOCIATED CONTENT

The Supporting Information is available free of charge on the ACS Publications website.

Table S1 gives the list of crystallographic parameters for ε-CL-20 (experimental and computational); Table S2 gives absolute values of six N-NO_2 wag angles of ε-CL-20 at high pressures; Table S3 gives assignment of the DFT-D computed fundamental eigenvectors for ε-CL-20; Table S4 compares the computationally calculated fundamental modes for ε-CL-20 to the INS spectrum reported in this work; variations of unit cell parameters of ε-CL-20 with pressure, are given in Table S5 (DFT-D), S6 (XRD) and S7 (NPD).

Figure S1 displays changes of wag angles with pressure; Figure S2 shows the computed phonon density of states; Rietveld refinement plots at elevated pressures are shown in Figure S3 (XRD) and S5 (NPD); Figure S4 compares calculated XRPD patterns of ε- and γ- form of CL-20; Figure S6 shows intermolecular distances monitored in the PIXEL calculations.

AUTHOR INFORMATION

Corresponding Author

*E-mail: sumit.konar@ed.ac.uk

ORCID

Sumit Konar: 0000-0003-3156-6536
Carole A. Morrison: 0000-0002-5489-7111
Colin Pulham: 0000-0002-3689-9594

Author Contributions

The manuscript was written through contributions of all authors. All authors have given approval to the final version of the manuscript.

Notes

The authors declare no competing financial interest. CCDC deposition numbers 2013605-2013621. Crystallographic information files are available free of charge from the Cambridge Crystallographic Data Center (CCDC) upon request (via www.ccdc.cam.ac.uk/data_request/cif, by emailing the data_request@ccdc.cam.ac.uk, or contacting The CCDC, 12 Union Road, Cambridge CB2 1EZ, UK; fax: + 44 1223 336033)

ACKNOWLEDGMENT

We are grateful to the UK Materials and Molecular Modelling Hub for computational resources, which is partially funded by EPSRC. Further thanks are given to the Edinburgh Compute and Data Facilities (ECDF) for additional computational resources. JGR gratefully acknowledges the University of Edinburgh for the award of a Principal's Career Development Scholarship. We are also thankful to Prof Simon Parsons and Mr. Matt Reeves for their help with MrPIXEL.

References

(1) Akhavan, J. *The Chemistry of Explosives*; 2011.

(2) Sikder, A. K.; Sikder, N. A Review of Advanced High Performance, Insensitive and Thermally Stable Energetic Materials Emerging for Military and Space Applications. *J. Hazard. Mater.* **2004**, *112* (1), 1–15. https://doi.org/10.1016/j.jhazmat.2004.04.003.

(3) Hunter, S.; Coster, P. L.; Davidson, A. J.; Millar, D. I. A.; Parker, S. F.; Marshall, W. G.; Smith, R. I.; Morrison, C. A.; Pulham, C. R. High-Pressure Experimental and DFT-D Structural Studies of the Energetic Material FOX-7. *J. Phys. Chem. C* **2015**, *119* (5), 2322–2334. https://doi.org/10.1021/jp5110888.

(4) Yoo, C.-S.; Cynn, H. Equation of State, Phase Transition, Decomposition of β-HMX (Octahydro-1,3,5,7-Tetranitro-1,3,5,7-Tetrazocine) at High Pressures. *J. Chem. Phys.* **1999**, *111* (22), 10229–10235. https://doi.org/10.1063/1.480341.

(5) Goetz, F.; Brill, T. B.; Ferraro, J. R. Pressure Dependence of the Raman and Infrared Spectra of .Alpha.-, .Beta.-, .Gamma.-, and .Delta.-Octahydro-1,3,5,7-Tetranitro-1,3,5,7-

Tetrazocine. *J. Phys. Chem.* **1978**, *82* (17), 1912–1917. https://doi.org/10.1021/j100506a011.

(6) Oswald, I. D. H.; Millar, D. I. A.; Davidson, A. J.; Francis, D. J.; Marshall, W. G.; Pulham, C. R.; Cumming, A.; Lennie, A. R.; Warren, J. E. High-Pressure Structural Studies of Energetic Compounds. *High Press. Res.* **2010**, *30* (2), 280–291. https://doi.org/10.1080/08957951003757903.

(7) Dreger, Z. A.; Gupta, Y. M. Phase Diagram of Hexahydro-1,3,5-Trinitro-1,3,5-Triazine Crystals at High Pressures and Temperatures. *J. Phys. Chem. A* **2010**, *114* (31), 8099–8105. https://doi.org/10.1021/jp105226s.

(8) Millar, D. I. A.; Oswald, I. D. H.; Barry, C.; Francis, D. J.; Marshall, W. G.; Pulham, C. R.; Cumming, A. S. Pressure-Cooking of Explosives—the Crystal Structure of ε-RDX as Determined by X-Ray and Neutron Diffraction. *Chem. Commun.* **2010**, *46* (31), 5662–5664. https://doi.org/10.1039/C0CC00368A.

(9) Stevens, L. L.; Velisavljevic, N.; Hooks, D. E.; Dattelbaum, D. M. Hydrostatic Compression Curve for Triamino-Trinitrobenzene Determined to 13.0 GPa with Powder X-Ray Diffraction. *Propellants Explos. Pyrotech.* **2008**, *33* (4), 286–295. https://doi.org/10.1002/prep.200700270.

(10) Nielsen, A. T.; Chafin, A. P.; Christian, S. L.; Moore, D. W.; Nadler, M. P.; Nissan, R. A.; Vanderah, D. J.; Gilardi, R. D.; George, C. F.; Flippen-Anderson, J. L. Synthesis of Polyazapolycyclic Caged Polynitramines. *Tetrahedron* **1998**, *54* (39), 11793–11812. https://doi.org/10.1016/S0040-4020(98)83040-8.

(11) Simpson, R. L.; Urtiew, P. A.; Ornellas, D. L.; Moody, G. L.; Scribner, K. J.; Hoffman, D. M. CL-20 Performance Exceeds That of HMX and Its Sensitivity Is Moderate. *Propellants Explos. Pyrotech.* **1997**, *22* (5), 249–255. https://doi.org/10.1002/prep.19970220502.

(12) Bazaki, H.; Kawabe, S.; Miya, H.; Kodama, T. Synthesis and Sensitivity of Hexanitrohexaaza-Isowurtzitane(HNIW). *Propellants Explos. Pyrotech.* **1998**, *23* (6), 333–336. https://doi.org/10.1002/(SICI)1521-4087(199812)23:6<333::AID-PREP333>3.0.CO;2-X.

(13) Foltz, M. F.; Coon, C. L.; Garcia, F.; Nichols, A. L. The Thermal Stability of the Polymorphs of Hexanitrohexaazaisowurtzitane, Part I. *Propellants Explos. Pyrotech.* **1994**, *19* (1), 19–25.

(14) Foltz, M. F.; Coon, C. L.; Garcia, F.; Nichols, A. L. The Thermal Stability of the Polymorphs of Hexanitrohexaazaisowurtzitane, Part II. *Propellants Explos. Pyrotech.* **1994**, *19* (3), 133–144.

(15) Nedelko, V. V.; Chukanov, N. V.; Raevskii, A. V.; Korsounskii, B. L.; Larikova, T. S.; Kolesova, O. I.; Volk, F. Comparative Investigation of Thermal Decomposition of Various Modifications of Hexanitrohexaazaisowurtzitane (CL-20). *Propellants Explos. Pyrotech.* **2000**, *25* (5), 255–259. https://doi.org/10.1002/1521-4087(200011)25:5<255::AID-PREP255>3.0.CO;2-8.

(16) Nair, U. R.; Sivabalan, R.; Gore, G. M.; Geetha, M.; Asthana, S. N.; Singh, H. Hexanitrohexaazaisowurtzitane (CL-20) and CL-20-Based Formulations (Review). *Combust. Explos. Shock Waves* **2005**, *41* (2), 121–132. https://doi.org/10.1007/s10573-005-0014-2.

(17) Russell, T. P.; Miller, P. J.; Piermarini, G. J.; Block, S. High-Pressure Phase Transition in. Gamma.-Hexanitrohexaazaisowurtzitane. *J. Phys. Chem.* **1992**, *96* (13), 5509–5512.

(18) Kholod, Y.; Okovytyy, S.; Kuramshina, G.; Qasim, M.; Gorb, L.; Leszczynski, J. An Analysis of Stable Forms of CL-20: A DFT Study of Conformational Transitions, Infrared and Raman Spectra. *J. Mol. Struct.* **2007**, *843* (1–3), 14–25. https://doi.org/10.1016/j.molstruc.2006.12.031.

(19) Millar, D. I. A.; Maynard-Casely, H. E.; Kleppe, A. K.; Marshall, W. G.; Pulham, C. R.; Cumming, A. S. Putting the Squeeze on Energetic Materials-Structural Characterisation of a High-Pressure Phase of CL-20. *Crystengcomm* **2010**, *12* (9), 2524–2527. https://doi.org/10.1039/c002701d.

(20) Fell, N. F.; Widder, J. M.; Medlin, S. V.; Morris, J. B.; Pesce-Rodriguez, R. A.; McNesby, K. L. Fourier TransformRaman Spectroscopy of Some Energetic Materials and Propellant Formulations. II. *J. Raman Spectrosc.* **1996**, *27* (2), 97–104. https://doi.org/10.1002/(SICI)1097-4555(199602)27:2<97::AID-JRS931>3.0.CO;2-P.

(21) McNesby, K. L.; Wolfe, J. E.; Morris, J. B.; Pesce-Rodriguez, R. A. Fourier Transform Raman Spectroscopy of Some Energetic Materials and Propellant Formulations. *J. Raman Spectrosc.* **1994**, *25* (1), 75–87. https://doi.org/10.1002/jrs.1250250111.

(22) Goede, P.; Latypov, N. V.; Östmark, H. Fourier Transform Raman Spectroscopy of the Four Crystallographic Phases of α, β, γ and ε 2,4,6,8,10,12-Hexanitro-2,4,6,8,10,12-Hexaazatetracyclo[5.5.0.05,9.03,11]Dodecane (HNIW, CL-20). *Propellants Explos. Pyrotech.* **2004**, *29* (4), 205–208. https://doi.org/10.1002/prep.200400047.

(23) He, X.; Liu, Y.; Huang, S.; Liu, Y.; Pu, X.; Xu, T. Raman Spectroscopy Coupled with Principal Component Analysis to Quantitatively Analyze Four Crystallographic Phases of Explosive CL-20. *RSC Adv.* **2018**, *8* (41), 23348–23352. https://doi.org/10.1039/C8RA02189A.

(24) Guo, R.; Tao, J.; Duan, X.-H.; Wu, C.; Li, H.-Z. Study on Phonon Spectra and Heat Capacities of CL-20/MTNP Cocrystal and Co-Formers by Density Functional Theory Method. *J. Mol. Model.* **2020**, *26* (6), 148. https://doi.org/10.1007/s00894-020-04415-3.

(25) Michalchuk, A. A. L.; Fincham, P. T.; Portius, P.; Pulham, C. R.; Morrison, C. A. A Pathway to the Athermal Impact Initiation of Energetic Azides. *J. Phys. Chem. C* **2018**, *122* (34), 19395–19408. https://doi.org/10.1021/acs.jpcc.8b05285.

(26) Michalchuk, A. A. L.; Trestman, M.; Rudić, S.; Portius, P.; Fincham, P. T.; Pulham, C. R.; Morrison, C. A. Predicting the Reactivity of Energetic Materials: An *Ab Initio* Multi-Phonon Approach. *J. Mater. Chem. A* **2019**, *7* (33),

19539–19553. https://doi.org/10.1039/C9TA06209B.

(27) Gump, J. C.; Peiris, S. M. Phase Transitions and Isothermal Equations of State of Epsilon Hexanitrohexaazaisowurtzitane (CL-20). *J. Appl. Phys.* **2008**, *104* (8), 083509. https://doi.org/10.1063/1.2990066.

(28) Ciezak, J. A.; Jenkins, T. A.; Liu, Z. Evidence for a High-Pressure Phase Transition of ε-2,4,6,8,10,12-Hexanitrohexaazaisowurtzitane (CL-20) Using Vibrational Spectroscopy. *Propellants Explos. Pyrotech.* **2007**, *32* (6), 472–477. https://doi.org/10.1002/prep.200700209.

(29) Millar, D. I. A. *Energetic Materials at Extreme Conditions*; Springer Theses; Springer-Verlag: Berlin Heidelberg, 2012. https://doi.org/10.1007/978-3-642-23132-2.

(30) Konar, S.; Michalchuk, A. A. L.; Sen, N.; Bull, C. L.; Morrison, C. A.; Pulham, C. R. High-Pressure Study of Two Polymorphs of 2,4,6-Trinitrotoluene Using Neutron Powder Diffraction and Density Functional Theory Methods. *J. Phys. Chem. C* **2019**. https://doi.org/10.1021/acs.jpcc.9b07658.

(31) Tan, J.-J.; Ji, G.-F.; Chen, X.-R.; Li, Z. Structure, Equation of State and Elasticity of Crystalline HNIW by Molecular Dynamics Simulations. *Phys. B Condens. Matter* **2011**, *406* (15), 2925–2930. https://doi.org/10.1016/j.physb.2011.03.062.

(32) Bidault, X.; Chaudhuri, S. A Flexible-Molecule Force Field to Model and Study Hexanitrohexaazaisowurtzitane (CL-20) – Polymorphism under Extreme Conditions. *RSC Adv.* **2019**, *9* (68), 39649–39661. https://doi.org/10.1039/C9RA07645J.

(33) Byrd, E. F. C.; Rice, B. M. Ab Initio Study of Compressed 1,3,5,7-Tetranitro-1,3,5,7-Tetraazacyclooctane (HMX), Cyclotrimethylenetrinitramine (RDX), 2,4,6,8,10,12-Hexanitrohexaazaisowurzitane (CL-20), 2,4,6-Trinitro-1,3,5-Benzenetriamine (TATB), and Pentaerythritol Tetranitrate (PETN). *J. Phys. Chem. C* **2007**, *111* (6), 2787–2796. https://doi.org/10.1021/jp0617930.

(34) Xu, X.-J.; Zhu, W.-H.; Xiao, H.-M. DFT Studies on the Four Polymorphs of Crystalline CL-20 and the Influences of Hydrostatic Pressure on ε-CL-20 Crystal. *J. Phys. Chem. B* **2007**, *111* (8), 2090–2097. https://doi.org/10.1021/jp066833e.

(35) Sorescu, D. C.; Rice, B. M. Theoretical Predictions of Energetic Molecular Crystals at Ambient and Hydrostatic Compression Conditions Using Dispersion Corrections to Conventional Density Functionals (DFT-D). *J. Phys. Chem. C* **2010**, *114* (14), 6734–6748. https://doi.org/10.1021/jp100379a.

(36) Zhong, M.; Qin, H.; Liu, Q.-J.; Liu, F.-S.; Tang, B. Structures, Elasticity, and Sensitivity Characteristics of ε-CL-20 under High Pressure from First-Principles Calculations. *Phys. Status Solidi B* **2019**, *256* (5), 1800440. https://doi.org/10.1002/pssb.201800440.

(37) Merrill, L.; Bassett, W. A. Miniature Diamond Anvil Pressure Cell for Single Crystal X-ray Diffraction Studies. *Rev. Sci. Instrum.* **1974**, *45* (2), 290–294. https://doi.org/10.1063/1.1686607.

(38) Piermarini, G. J.; Block, S.; Barnett, J. D.; Forman, R. A. Calibration of the Pressure Dependence of the R1 Ruby Fluorescence Line to 195 Kbar. *J. Appl. Phys.* **1975**, *46* (6), 2774–2780. https://doi.org/10.1063/1.321957.

(39) Angel, R. J.; Bujak, M.; Zhao, J.; Gatta, G. D.; Jacobsen, S. D. Effective Hydrostatic Limits of Pressure Media for High-Pressure Crystallographic Studies. *J. Appl. Crystallogr.* **2007**, *40* (1), 26–32. https://doi.org/10.1107/S0021889806045523.

(40) Hammersley, A. P.; Svensson, S. O.; Hanfland, M.; Fitch, A. N.; Hausermann, D. Two-Dimensional Detector Software: From Real Detector to Idealised Image or Two-Theta Scan. *High Press. Res.* **1996**, *14* (4–6), 235–248. https://doi.org/10.1080/08957959608201408.

(41) Larson, A. C.; Von Dreele, R. B. *General Structure Analysis System (GSAS)*; Los Alamos National Laboratory Report LAUR 86-748, 2004.

(42) Bull, C. L.; Funnell, N. P.; Tucker, M. G.; Hull, S.; Francis, D. J.; Marshall, W. G. PEARL: The High Pressure Neutron Powder Diffractometer at ISIS. *High Press. Res.* **2016**, *36* (4), 493–511. https://doi.org/10.1080/08957959.2016.1214730.

(43) Strässle, Th.; Klotz, S.; Kunc, K.; Pomjakushin, V.; White, J. S. Equation of State of Lead from High-Pressure Neutron Diffraction up to 8.9 GPa and Its Implication for the NaCl Pressure Scale. *Phys. Rev. B* **2014**, *90* (1), 014101. https://doi.org/10.1103/PhysRevB.90.014101.

(44) Besson, J. M.; Nelmes, R. J.; Hamel, G.; Loveday, J. S.; Weill, G.; Hull, S. Neutron Powder Diffraction above 10 GPa. *Phys. B Condens. Matter* **1992**, *180–181*, 907–910. https://doi.org/10.1016/0921-4526(92)90505-M.

(45) Arnold, O.; Bilheux, J. C.; Borreguero, J. M.; Buts, A.; Campbell, S. I.; Chapon, L.; Doucet, M.; Draper, N.; Ferraz Leal, R.; Gigg, M. A.; Lynch, V. E.; Markvardsen, A.; Mikkelson, D. J.; Mikkelson, R. L.; Miller, R.; Palmen, K.; Parker, P.; Passos, G.; Perring, T. G.; Peterson, P. F.; Ren, S.; Reuter, M. A.; Savici, A. T.; Taylor, J. W.; Taylor, R. J.; Tolchenov, R.; Zhou, W.; Zikovsky, J. Mantid—Data Analysis and Visualization Package for Neutron Scattering and μ SR Experiments. *Nucl. Instrum. Methods Phys. Res. Sect. Accel. Spectrometers Detect. Assoc. Equip.* **2014**, *764*, 156–166. https://doi.org/10.1016/j.nima.2014.07.029.

(46) Colognesi, D.; Celli, M.; Cilloco, F.; Newport, R. j.; Parker, S. f.; Rossi-Albertini, V.; Sacchetti, F.; Tomkinson, J.; Zoppi, M. TOSCA Neutron Spectrometer: The Final Configuration. *Appl. Phys. Mater. Sci. Process.* **2002**, *74* (6), s64. https://doi.org/10.1007/s003390101078.

(47) Ramirez-Cuesta, A. J. ACLIMAX 4.0.1, The New Version of the Software for Analyzing and Interpreting INS Spectra. *Comput. Phys. Commun.* **2004**, *157* (3), 226–238. https://doi.org/10.1016/S0010-4655(03)00520-4.

(48) Clark, S. J.; Segall, M. D.; Pickard, C. J.; Hasnip, P. J.; Probert, M. I. J.; Refson, K.; Payne, M. C. First Principles Methods Using CASTEP. *Z. Für Krist. - Cryst. Mater.* **2005**, *220* (5/6), 567–570. https://doi.org/10.1524/zkri.220.5.567.65075.

(49) Grimme, S. Semiempirical GGA-Type Density Functional Constructed with a Long-Range Dispersion Correction. *J. Comput. Chem.* **2006**, *27* (15), 1787–1799. https://doi.org/10.1002/jcc.20495.

(50) Perdew, J. P.; Burke, K.; Ernzerhof, M. Generalized Gradient Approximation Made Simple. *Phys. Rev. Lett.* **1996**, *77* (18), 3865–3868. https://doi.org/10.1103/PhysRevLett.77.3865.

(51) Vackář, J.; Hyt'ha, M.; Šimůnek, A. All-Electron Pseudopotentials. *Phys. Rev. B* **1998**, *58* (19), 12712–12720. https://doi.org/10.1103/PhysRevB.58.12712.

(52) Monkhorst, H. J.; Pack, J. D. Special Points for Brillouin-Zone Integrations. *Phys. Rev. B Solid State* **1976**, *13* (12), 5188–5192. https://doi.org/10.1103/PhysRevB.13.5188.

(53) Fischer, T. H.; Almlof, J. General Methods for Geometry and Wave Function Optimization. *J. Phys. Chem.* **1992**, *96* (24), 9768–9774. https://doi.org/10.1021/j100203a036.

(54) Gavezzotti, A. Calculation of Lattice Energies of Organic Crystals: The PIXEL Integration Method in Comparison with More Traditional Methods. *Z. Für Krist. - Cryst. Mater.* **2009**, *220* (5/6), 499–510. https://doi.org/10.1524/zkri.220.5.499.65063.

(55) Wood, P. A.; Francis, D.; Marshall, W. G.; Moggach, S. A.; Parsons, S.; Pidcock, E.; Rohl, A. L. A Study of the High-Pressure Polymorphs of L-Serine Using Ab Initio Structures and PIXEL Calculations. *CrystEngComm* **2008**, *10* (9), 1154–1166. https://doi.org/10.1039/B801571F.

(56) Wood, P. A.; Forgan, R. S.; Henderson, D.; Parsons, S.; Pidcock, E.; Tasker, P. A.; Warren, J. E. Effect of Pressure on the Crystal Structure of Salicylaldoxime-I, and the Structure of Salicylaldoxime-II at 5.93 GPa. *Acta Crystallogr. B* **2006**, *62* (6), 1099–1111. https://doi.org/10.1107/S0108768106031752.

(57) Gavezzotti, A. Efficient Computer Modeling of Organic Materials. The Atom–Atom, Coulomb–London–Pauli (AA-CLP) Model for Intermolecular Electrostatic-Polarization, Dispersion and Repulsion Energies. *New J. Chem.* **2011**, *35* (7), 1360–1368. https://doi.org/10.1039/C0NJ00982B.

(58) Reeves, M.; Parsons, S.; Wood, P. MR_PIXEL (Manuscript in Preparation).

(59) M. J. Frisch, G. W. Trucks, H. B. Schlegel, G. E. Scuseria, M. A. Robb, J. R. Cheeseman, G. Scalmani, V. Barone, G. A. Petersson, H. Nakatsuji, X. Li, M. Caricato, A. Marenich, J. Bloino, B. G. Janesko, R. Gomperts, B. Mennucci, H. P. Hratchian, J. V. Ortiz, A. F. Izmaylov, J. L. Sonnenberg, D. Williams-Young, F. Ding, F. Lipparini, F. Egidi, J. Goings, B. Peng, A. Petrone, T. Henderson, D. Ranasinghe, V. G. Zakrzewski, J. Gao, N. Rega, G. Zheng, W. Liang, M. Hada, M. Ehara, K. Toyota, R. Fukuda, J. Hasegawa, M. Ishida, T. Nakajima, Y. Honda, O. Kitao, H. Nakai, T. Vreven, K. Throssell, J. A. Montgomery, Jr., J. E. Peralta, F. Ogliaro, M. Bearpark, J. J. Heyd, E. Brothers, K. N. Kudin, V. N. Staroverov, T. Keith, R. Kobayashi, J. Normand, K. Raghavachari, A. Rendell, J. C. Burant, S. S. Iyengar, J. Tomasi, M. Cossi, J. M. Millam, M. Klene, C. Adamo, R. Cammi, J. W. Ochterski, R. L. Martin, K. Morokuma, O. Farkas, J. B. Foresman, and D. J. Fox. *Gaussian 09, Revision A.02, , Gaussian, Inc.*; Wallingford CT, 2016.

(60) Bolotina, N. B.; Hardie, M. J.; Speer Jr, R. L.; Pinkerton, A. A. Energetic Materials: Variable-Temperature Crystal Structures of γ- and ϵ-HNIW Polymorphs. *J. Appl. Crystallogr.* **2004**, *37* (5), 808–814. https://doi.org/10.1107/S0021889804017832.

(61) Sun, X.; Sui, Z.; Wang, J.; Li, X.; Wang, X.; Dai, R.; Wang, Z.; Huang, S.; Zhang, Z. Phase Transition Routes for ε- and γ-CL-20 Crystals under High Pressures of up to 60 GPa. *J. Phys. Chem. C* **2020**, *124* (9), 5061–5068. https://doi.org/10.1021/acs.jpcc.9b11224.

(62) Christensen, J.; Horton, P. N.; Bury, C. S.; Dickerson, J. L.; Taberman, H.; Garman, E. F.; Coles, S. J. Radiation Damage in Small-Molecule Crystallography: Fact Not Fiction. *IUCrJ* **2019**, *6* (4), 703–713. https://doi.org/10.1107/S2052252519006948.

(63) Wood, P. A.; Haynes, D. A.; Lennie, A. R.; Motherwell, W. D. S.; Parsons, S.; Pidcock, E.; Warren, J. E. The Anisotropic Compression of the Crystal Structure of 3-Aza-Bicyclo(3.3.1)Nonane-2,4-Dione to 7.1 GPa. *Cryst. Growth Des.* **2008**, *8* (2), 549–558. https://doi.org/10.1021/cg0705815.

SUPPORTING INFORMATION

High-Pressure Neutron Powder Diffraction Study of ε-CL-20: A Gentler Way to Study Energetic Materials

Sumit Konar,*† Steven Hunter,† Carole A. Morrison,† Paul L. Coster,† Helen E. Maynard-Casely,† Jonathan G. Richardson,† William G. Marshall,‡ Annette Kleppe,§ Stewart F. Parker,‡ and Colin R. Pulham*†

†EaStCHEM School of Chemistry and Centre for Science at Extreme Conditions, The University of Edinburgh, King's Buildings, David Brewster Road, Edinburgh EH9 3FJ, U.K.

‡ISIS Neutron and Muon Facility, STFC Rutherford Appleton Laboratory, Harwell, Oxford, Didcot, Oxfordshire OX11 0QX, U.K.

§ Diamond Light Source, Rutherford Appleton Laboratory, Harwell Science and Innovation Campus, Didcot, Oxfordshire, OX110QX, England, U.K.

(*E-mail: sumit.konar@ed.ac.uk; c.r.pulham@ed.ac.uk)

Table S1: Comparison of the crystallographic parameters for ε-CL-20 calculated at ambient pressure using the DFT-D method alongside results obtained from previous experimental and computational studies.

Parameter	Exp.[1]	Exp[2]	DFT-D[3]	DFT-D[4]	NPT-MD[5]	MD[6]
a (Å)	8.863(1)	8.852(2)	8.9189	8.9157	8.815	8.951
b (Å)	12.593(2)	12.556(3)	12.6706	12.5171	12.526	12.284
c (Å)	13.395(2)	13.386(3)	13.4251	13.4132	13.319	13.437
β (deg.)	106.920(2)	106.82(2)	106.559	106.58	106.82	104.95
V (Å^3)	1430.2(3)	1424.2(5)	1454.23	1434.68	1407.80	1427.44

[1] Bolotina et al.. J. Appl. Crystallogr. 2004, 37 (5), 808–814.
[2] Nielsen et al. Tetrahedron 1998, 54 (39), 11793–11812.
[3] Konar et al. (this work)
[4] Sorescu et al. J. Phys. Chem. C 2010, 114 (14), 6734–6748.
[5] Tan et al. Phys. B Condens. Matter 2011, 406 (15), 2925–2930.
[6] Bidault et al. RSC Adv. 2019, 9 (68), 39649–39661.

Figure S1 a) Definition of wag angle (δ); b) changes of wag angles with pressure; the values are obtained from DFT calculations

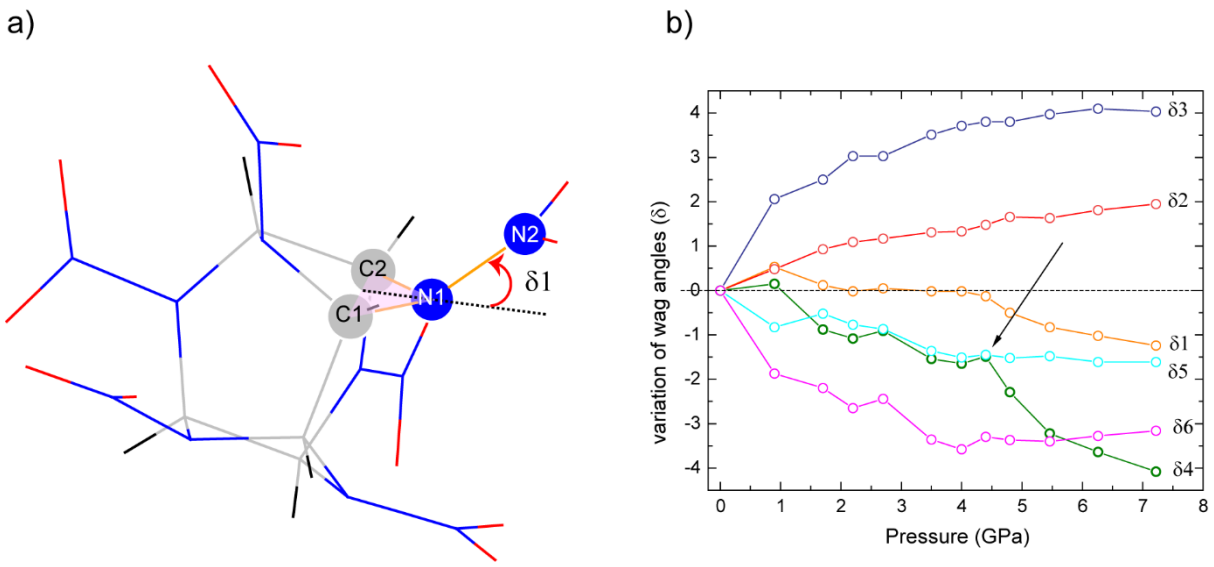

Table S2 Absolute values of six N-NO_2 wag angles of ε-CL-20 at high pressures.

	Wag angle (deg)					
Pressure (GPa)	δ1	δ2	δ3	δ4	δ5	δ6
ambient	36.23	1.05	28.38	29.63	19.39	37.04
0.9	36.76	1.53	30.44	29.78	18.56	35.17
1.7	36.35	1.98	30.88	28.75	18.87	34.84
2.2	36.21	2.14	31.41	28.55	18.62	34.39
2.7	36.28	2.22	31.41	28.72	18.52	34.6
3.5	36.21	2.36	31.89	28.09	18.03	33.68
4	36.21	2.38	32.09	27.98	17.88	33.46
4.4	36.1	2.53	32.18	28.14	17.94	33.74
4.8	35.73	2.71	32.18	27.34	17.87	33.67
5.46	35.4	2.68	32.35	26.41	17.91	33.64
6.26	35.21	2.86	32.48	25.99	17.78	33.76
7.22	34.99	3	32.41	25.55	17.78	33.88

TABLE S3 Assignment of the DFT-D computed fundamental eigenvectors computed for ε-CL-20.

Mode no.	ν/cm^{-1} (calculated)	Assignment
1-3	0	Acoustic
4-22	32.5-70.0	Lattice modes
23-79	77.5-173.8	Lattice modes + amalgamated NO_2 wags/bends
79-100	193.3-259.4	Cage deformation bends + NO_2 wags/bends
101-112	292.6-308.6	Cage deformation str + N-N str
113-116	336.5-339.0	Cage deformation str
117-128	358.0-375.5	Cage deformation bend
129-132	396.9-398.2	Cage deformation bend + NO_2 bend
133-140	439.3-459.5	Cage N oop
141-149	515.9-566.8	Cage deformation bend + NO_2 bend
150-180	567.8-687.8	Cage deformation bend and twist
181-212	701.2-729.9	Cage deformation str and bend + NO_2 bends
213-384	764.8-1376.3	Whole molecule vibration
385-408	1636.5-1712.8	N-O str
409-432	3074.3-3100.9	C-H str

Figure S2 Computed phonon density of states (Brillouin zone Γ-point) for ε-CL-20

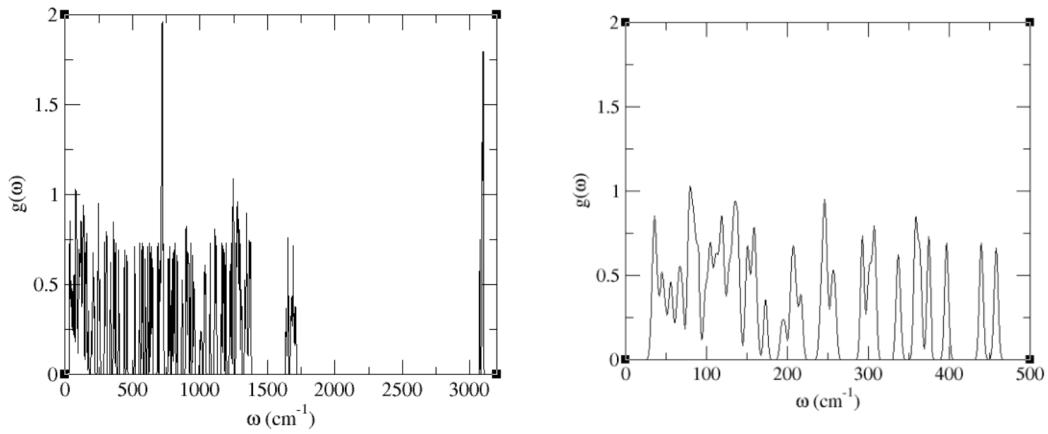

TABLE S4 Comparison of the computationally calculated fundamental modes for ε-CL-20 compared to the INS spectrum reported in this work. * Where there are multiple modes, the DFT-D value stated is an average of the contributing modes. All frequencies, ν, are in units of cm^{-1}.

Mode*	comp	INS	Mode*	comp	INS
4,5	33.8	28	97-100	257.3	266
6,7,8,9	36.7	33	101-104	293.4	306
10	41.2	40	105-108	302	314
11	44.2	43	109-112	307.9	318
12	45.3	46	113,114	336.7	339
13	47.3	50	115,116	338.7	349
14	50.9	53	117-124	360.9	376
15,16	55.5	57	125-128	374.8	386
17	58.1	61	129-132	397.3	412
18	63.4	65	133-136	440.1	450
19,20	66.2	69	137-140	458.5	469
21,22	69.5	72	141-144	516.7	528
23,24	77.6	78	145-148	553.3	572
25-28	79.8	84	149-152	567.8	584
29-33	84.8	88	153-156	575.3	595
34-36	90.3	93	157-160	593.5	607
37,38	99.1	103	161-164	613.1	629
39,40	103.4	105	165-172	633.2	648
40-42	104.8	109	173-176	647	665
43,44	109.4	111	177-180	687.2	681
45,46	112.7	116	181-188	706	709
47,48	115.7	119	189-200	717.1	727
49-52	119.4	126	201-212	724.4	753
53	123	136	213-216	765.9	796
54-56	128.2	139	217-220	776.6	808
57-59	132.8	145	221-232	804.1	836
60-62	135.5	149	233-236	830.4	862
63-64	139.2	152	237-240	867.7	888
65-66	140.7	156	257-260	931.2	924
67-70	151.1	164	241-256	905.1	947
71,72	156.4	169	261-268	952.5	991
73-75	159.4	173	269,270	1001.6	1021
76	162.5	177	271,272	1011.1	1031
77	172.8	183	273-280	1035.1	1057
78	173.8	188	281-284	1075.9	1095
79	193.3	194	285-296	1114.8	1145
80	197.3	199	297-312	1175.3	1222
81-84	206.5	214	313-332	1238.3	1259
85,86	211.2	226	333-360	1284.4	1310
87-88	216.8	233	361-372	1341.2	1351
89-92	244	253	373-384	1369	1391
93-96	248.2	262	409-432	3092.2	3060

Table S5. Variation of unit cell parameters of ε-CL-20 with pressure, obtained from DFT calculations.

Pressure. (GPa)	a (Å)	b (Å)	c (Å)	β (deg)	V (Å^3)
0	8.9189	12.6706	13.4251	106.5587	1454.22
0.9(2)	8.7538	12.3403	13.1587	105.6479	1368.78
1.7(2)	8.678	12.0989	13.004	104.7637	1320.27
2.2(2)	8.6301	12.0148	12.9315	104.5233	1298.01
2.7(2)	8.593	11.9559	12.873	104.5745	1279.98
3.5(2)	8.5501	11.8325	12.7629	104.2722	1251.36
4.0(2)	8.5216	11.7742	12.7086	104.1699	1236.32
4.4(2)	8.4949	11.7397	12.6778	104.1666	1225.88
4.8(2)	8.4873	11.669	12.6277	103.8418	1214.31
5.46(2)	8.4613	11.5961	12.5691	103.5512	1198.92
6.26(2)	8.4297	11.5285	12.5076	103.4357	1182.24
7.22(2)	8.4018	11.4546	12.4338	103.3928	1164.08

Figure S3 Rietveld refinement plots of X-ray powder diffraction patterns at elevated pressures [λ = 0.4847 Å (up to 7.2 GPa) and λ = 0.3727 Å (above 7.2 GPa)]

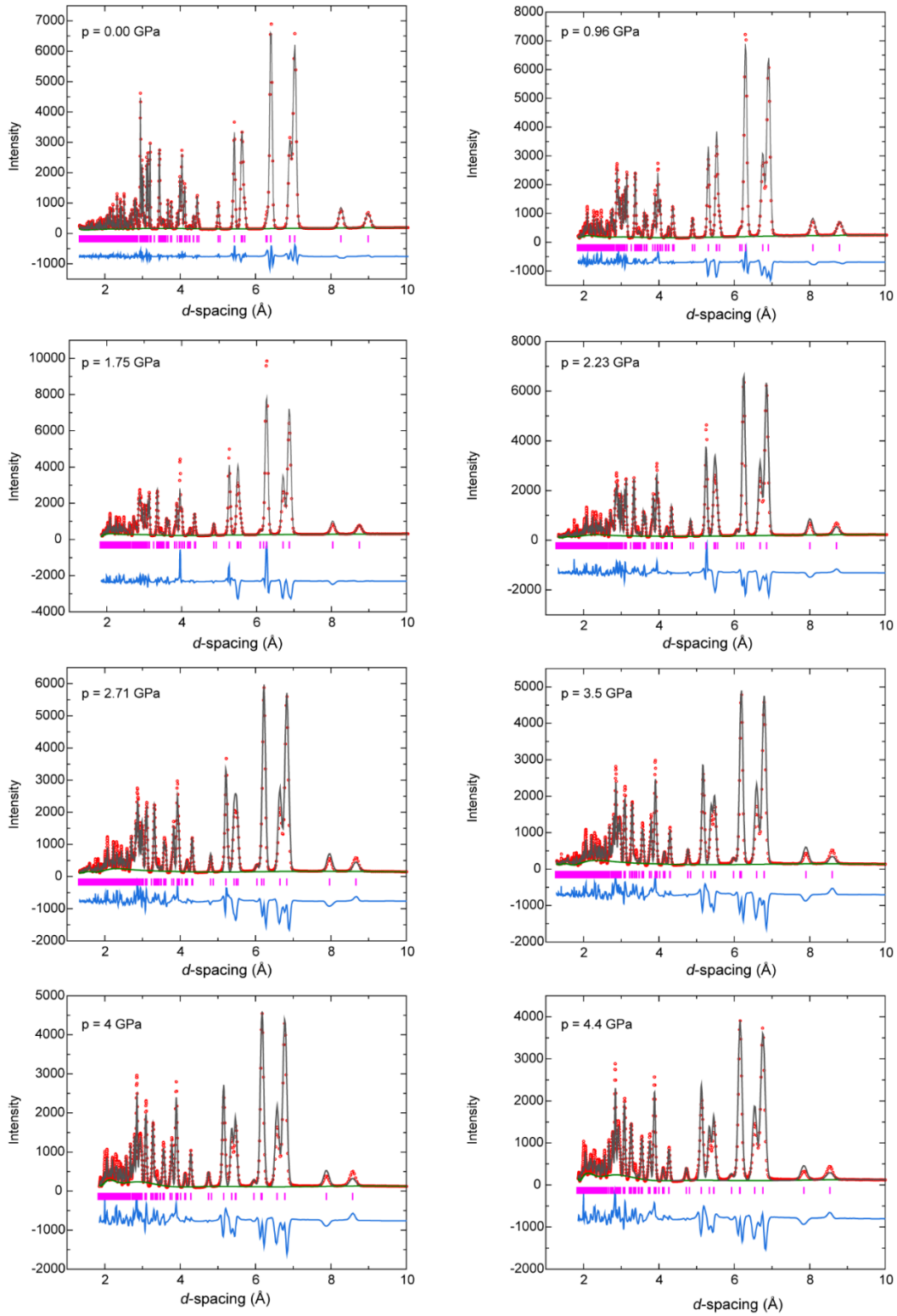

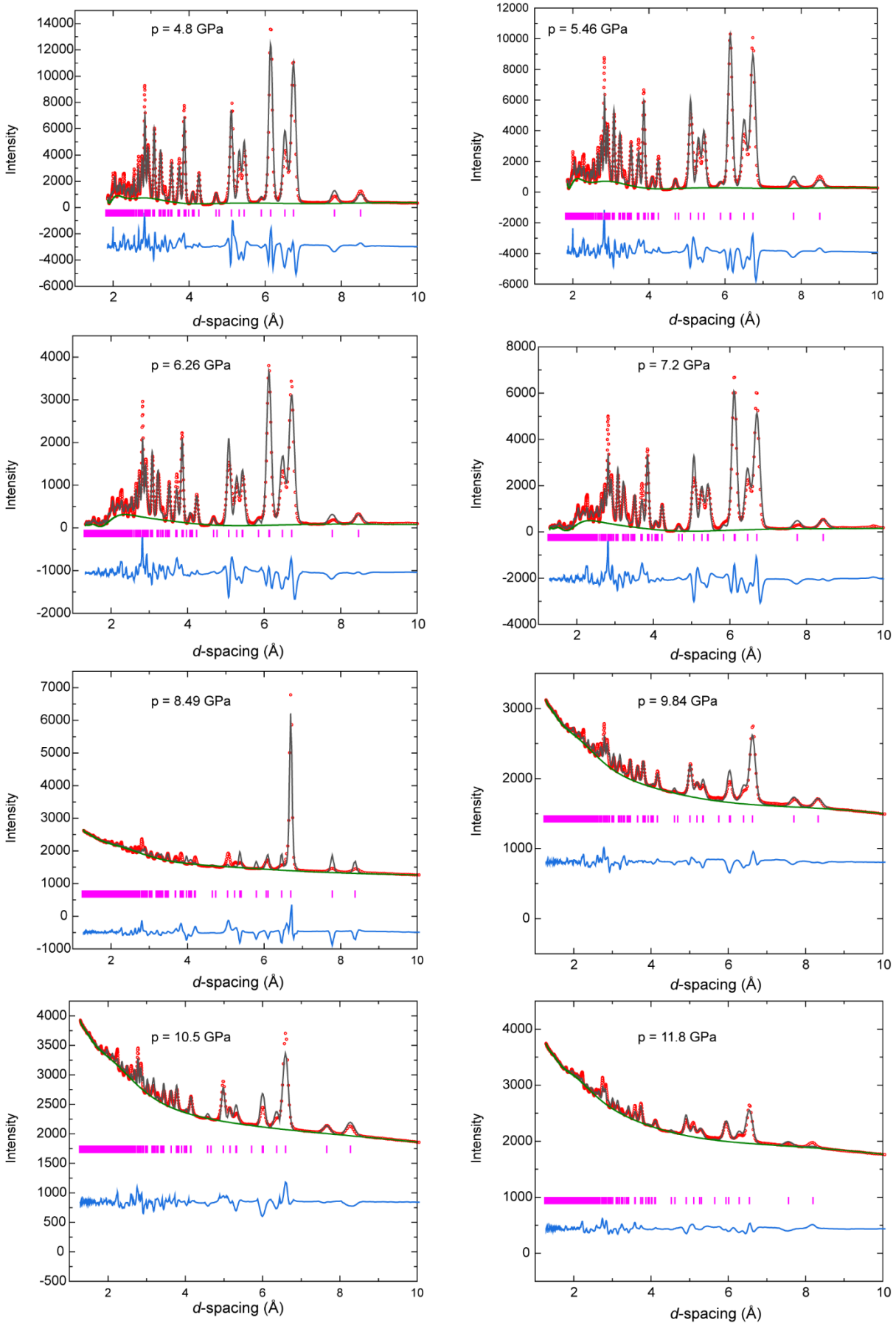
p = 4.8 GPa
p = 5.46 GPa
p = 6.26 GPa
p = 7.2 GPa
p = 8.49 GPa
p = 9.84 GPa
p = 10.5 GPa
p = 11.8 GPa
Intensity
d-spacing (Å)

Figure S4 Comparison of calculated XRPD patterns of ε- and γ- form of CL-20

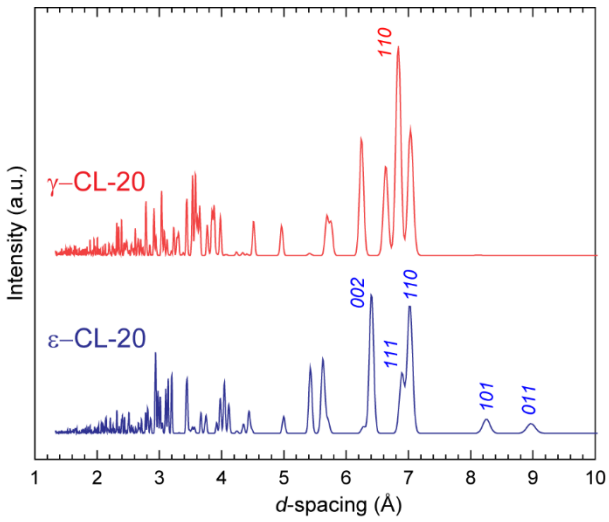

Figure S5 Rietveld refinement plots of Neutron powder diffraction patterns at elevated pressures

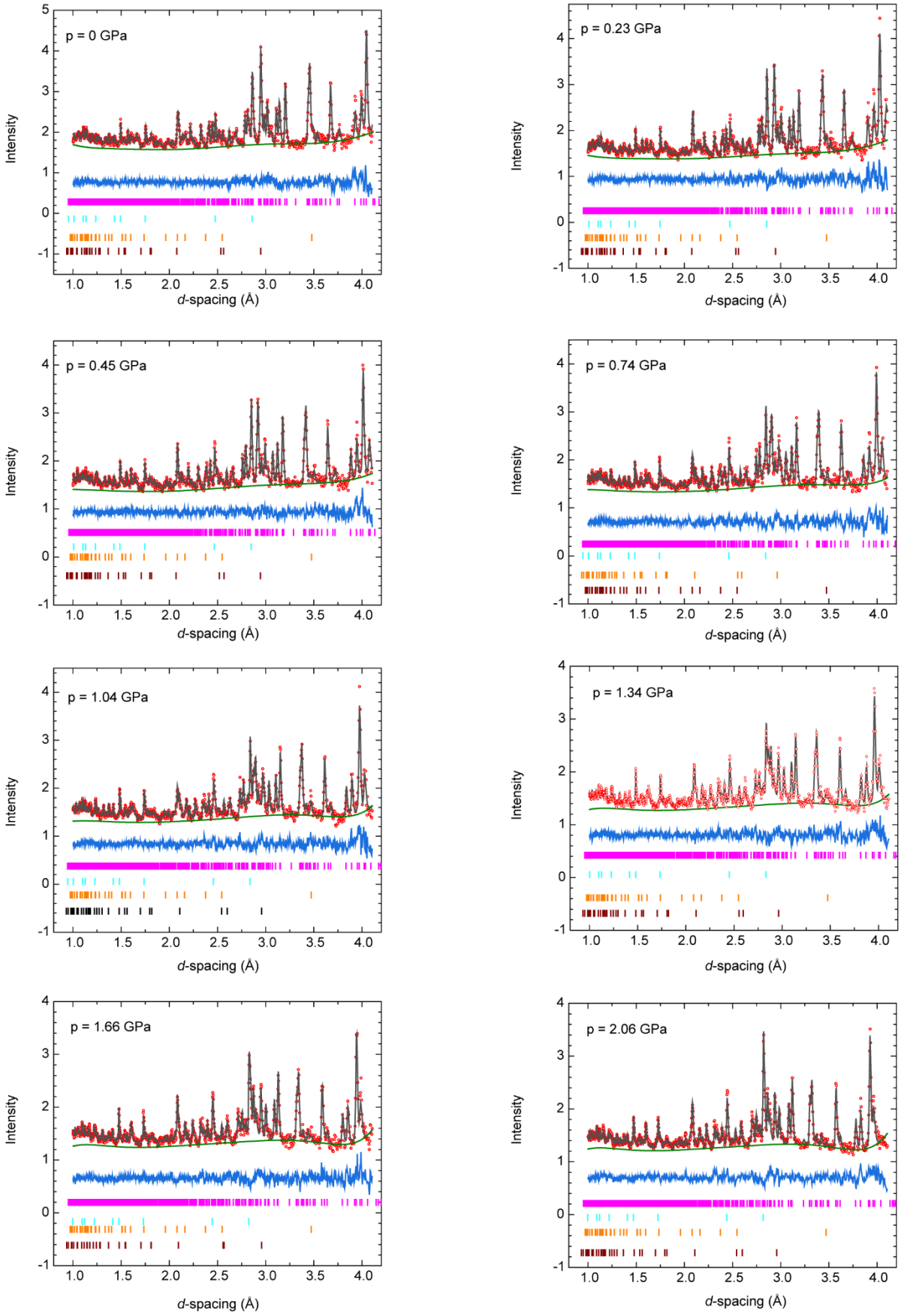

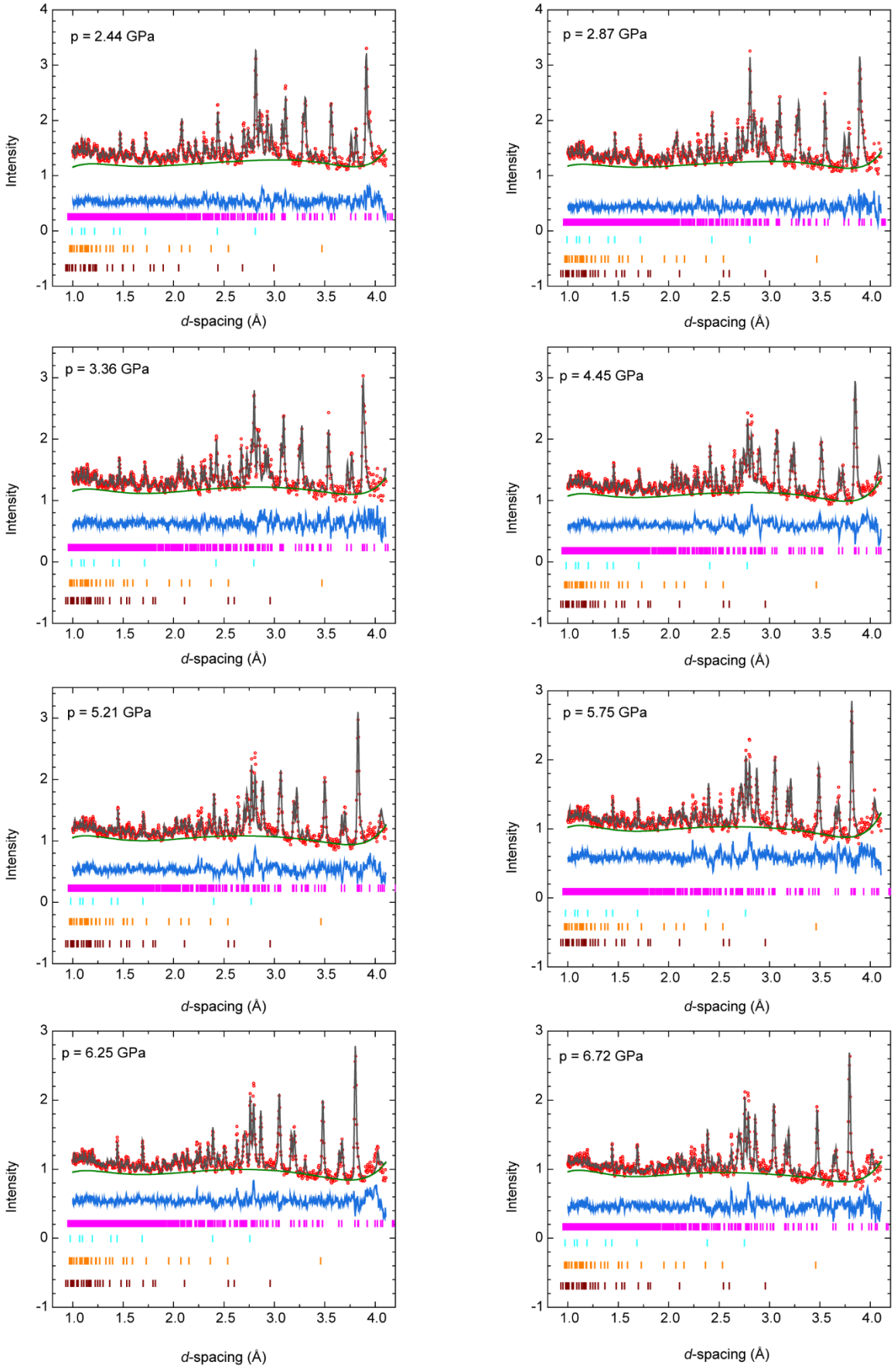
p = 2.44 GPa
p = 2.87 GPa
p = 3.36 GPa
p = 4.45 GPa
p = 5.21 GPa
p = 5.75 GPa
p = 6.25 GPa
p = 6.72 GPa
Intensity
d-spacing (Å)

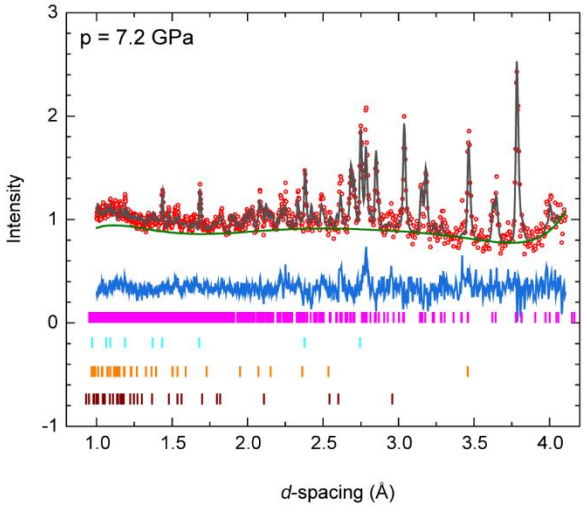
p = 7.2 GPa
Intensity
d-spacing (Å)
3
2
1
0
-1
1.0
1.5
2.0
2.5
3.0
3.5
4.0

Table S6. Variation of unit cell parameters of ε-CL-20 with pressure obtained from Rietveld refinement of XRPD patterns. Values in parentheses are estimated standard deviations. Values in regular and italic font indicate input structures for refinement are taken from CCDC 117779 [Nielsen, A. T. et al. Tetrahedron 54, 11793–11812 (1998)] and DFT optimised structures (this work), respectively.

Pressure. (GPa)	a (Å)	b (Å)	c (Å)	β (deg)	V (Å^3)	wRp
0	8.8669(2)	12.6023(3)	13.3916(3)	106.891(2)	1431.87(4)	0.0606
	8.8669(3)	*12.6022(4)*	*13.3913(3)*	*106.890(2)*	*1431.83(4)*	*0.0669*
0.9(2)	8.6987(8)	12.291(1)	13.121(1)	106.331(7)	1346.3(1)	0.119
	8.6977(6)	*12.2913(8)*	*13.1224(8)*	*106.325(5)*	*1346.3(1)*	*0.0886*
1.7(2)	8.660(1)	12.201(1)	13.044(1)	106.09(1)	1324.2(2)	0.1497
	8.6585(9)	*12.201(1)*	*13.048(1)*	*106.089(9)*	*1324.4(2)*	*0.1341*
2.2(2)	8.637(1)	12.149(1)	12.999(1)	105.964(9)	1311.3(2)	0.1675
	8.6348(7)	*12.149(1)*	*13.002(1)*	*105.956(7)*	*1311.4(1)*	*0.1366*
2.7(2)	8.603(1)	12.070(2)	12.927(1)	105.74(1)	1291.9(2)	0.1696
	8.6003(7)	*12.070(1)*	*12.931(1)*	*105.749(7)*	*1291.9(1)*	*0.1150*
3.5(2)	8.556(1)	11.959(2)	12.829(2)	105.39(1)	1265.7(2)	0.191
	8.5525(8)	*11.962(1)*	*12.833(1)*	*105.393(8)*	*1265.9(2)*	*0.1393*
4.0(2)	8.541(2)	11.915(2)	12.795(2)	105.25(2)	1256.3(3)	0.2021
	8.536(1)	*11.920(2)*	*12.799(2)*	*105.25(1)*	*1256.4(2)*	*0.1490*
4.4(2)	8.518(2)	11.848(3)	12.742(2)	105.04(2)	1241.9(3)	0.2086
	8.515(1)	*11.845(2)*	*12.745(2)*	*105.00(1)*	*1241.7(2)*	*0.1349*
4.8(2)	8.506(2)	11.801(3)	12.716(2)	104.88(2)	1233.7(3)	0.2038
	8.504(1)	*11.793(2)*	*12.718(2)*	*104.82(2)*	*1233.0(2)*	*0.1468*
5.46(2)	8.49214	11.760(4)	12.687(3)	104.68(2)	1225.6(4)	0.2065
	8.489(2)	*11.753(3)*	*12.687(2)*	*104.62(2)*	*1224.7(3)*	*0.1700*
6.26(2)	8.477(2)	11.713(4)	12.658(2)	104.52(2)	1216.7(4)	0.2006
	8.474(2)	*11.702(3)*	*12.659(2)*	*104.48(2)*	*1215.5(3)*	*0.1694*
7.22(2)	8.461(3)	11.672(4)	12.624(3)	104.43(2)	1207.3(4)	0.2099
	8.455(2)	*11.662(3)*	*12.629(2)*	*104.41(2)*	*1206.2(3)*	*0.1744*
8.49(2)	8.486(3)	11.591(9)	12.527(7)	104.85(4)	1191.0(8)	0.0345
9.84(2)	8.384(3)	11.504(6)	12.473(4)	104.79(3)	1163.2(5)	0.0147
10.5(5)	8.346(4)	11.430(7)	12.396(5)	104.78(4)	1143.3(5)	0.0175
11.8(5)	8.274(4)	11.300(7)	12.251(5)	104.05(5)	1111.3(7)	0.0125

Table S7. Variation of unit cell parameters of ε-CL-20 with pressure, obtained from Rietveld refinement of NPD patterns. Values in parentheses are estimated standard deviations. Values in regular and italic font indicate input structures for refinement are taken from CCDC 117779 [Nielsen, A. T. et al. Tetrahedron 54, 11793–11812 (1998)] and DFT optimised structures (this work), respectively.

Pressure.(GPa)	a (Å)	b (Å)	c (Å)	β (deg)	V (Å^3)	wRp
0.00(1)	8.8629(9)	12.596(2)	13.380(1)	106.917(8)	1429.0(2)	0.0229
	8.863(1)	*12.595(2)*	*13.379(1)*	*106.913(8)*	*1428.9(2)*	*0.0230*
0.22(1)	8.8138(9)	12.510(2)	13.311(2)	106.742(8)	1405.6(2)	0.0253
	8.814(1)	*12.510(2)*	*12.311(2)*	*106.738(8)*	*1405.5(2)*	*0.0251*
0.43(1)	8.7739(8)	12.443(1)	13.253(1)	106.608(8)	1386.5(2)	0.0242
	8.7736(8)	*12.442(1)*	*13.252(1)*	*106.604(8)*	*1386.3(2)*	*0.0238*
0.71(1)	8.7295(9)	12.354(1)	13.181(2)	106.405(9)	1363.6(2)	0.0267
	8.7291(8)	*12.354(1)*	*13.181(1)*	*106.407(8)*	*1363.5(2)*	*0.0240*
1.01(1)	8.6906(9)	12.277(1)	13.111(1)	106.229(8)	1343.1(2)	0.0269
	8.690(1)	*12.277(1)*	*13.112(1)*	*106.232(7)*	*1343.0(2)*	*0.0236*
1.31(1)	8.6571(9)	12.205(1)	13.049(1)	106.081(9)	1324.8(2)	0.0263
	8.6567(7)	*12.204(1)*	*13.050(1)*	*106.081(8)*	*1324.7(2)*	*0.0231*
1.63(1)	8.6238(9)	12.139(2)	12.992(2)	105.903(9)	1307.9(2)	0.0282
	8.6236(8)	*12.137(1)*	*12.993(1)*	*105.900(8)*	*1307.9(2)*	*0.0246*
2.04(1)	8.5912(8)	12.063(1)	12.928(1)	105.713(8)	1289.7(2)	0.0261
	8.5912(6)	*12.063(1)*	*12.929(1)*	*105.716(6)*	*1289.8(1)*	*0.0197*
2.40(1)	8.5607(9)	11.994(2)	12.866(2)	105.527(9)	1272.9(2)	0.0294
	8.5613(7)	*11.995(1)*	*12.869(1)*	*105.544(7)*	*1273.2(1)*	*0.0230*
2.83(1)	8.5322(9)	11.925(2)	12.808(2)	105.37(1)	1256.6(2)	0.0315
	8.5324(7)	*11.926(1)*	*12.810(1)*	*105.373(8)*	*1256.8(2)*	*0.0252*
3.34(1)	8.500(1)	11.854(2)	12.742(2)	105.15(1)	1239.3(2)	0.0342
	8.5016(8)	*11.855(1)*	*12.743(1)*	*105.157(9)*	*1239.6(2)*	*0.0286*
4.44(2)	8.448(1)	11.724(2)	12.621(2)	104.80(1)	1208.6(2)	0.0314
	8.4474(7)	*11.723(1)*	*12.622(1)*	*104.79(1)*	*1208.5(1)*	*0.0209*
5.20(2)	8.416(1)	11.642(2)	12.547(2)	104.60(1)	1189.6(2)	0.0357
	8.4145(7)	*11.640(1)*	*12.547(1)*	*104.59(1)*	*1189.4(1)*	*0.0236*
5.75(2)	8.394(1)	11.592(2)	12.501(2)	104.49(2)	1177.7(2)	0.0409
	8.3933(8)	*11.590(2)*	*12.501(1)*	*104.48(1)*	*1177.4(2)*	*0.0280*
6.24(2)	8.373(1)	11.549(2)	12.455(1)	104.33(1)	1167.0(2)	0.0313
	8.3735(7)	*11.547(1)*	*12.456(1)*	*104.33(1)*	*1166.9(1)*	*0.0228*
6.70(2)	8.360(1)	11.509(2)	12.422(2)	104.25(2)	1158.4(2)	0.0412
	8.3595(8)	*11.506(2)*	*12.421(1)*	*104.24(1)*	*1158.1(2)*	*0.0285*
7.18(3)	8.344(2)	11.472(3)	12.391(2)	104.18(2)	1149.9(3)	0.0494
	8.344(1)	*11.469(2)*	*12.391(2)*	*104.18(1)*	*1149.7(2)*	*0.0375*

Figure S6 Intermolecular distances (d1-d8) monitored in the PIXEL calculations. The distances quoted here are obtained from computational cif file at ambient pressure.